Improving the stability and opto-electrical properties of hydrogenated amorphous and nano-crystalline germanium films

J.E.C. van Dingen

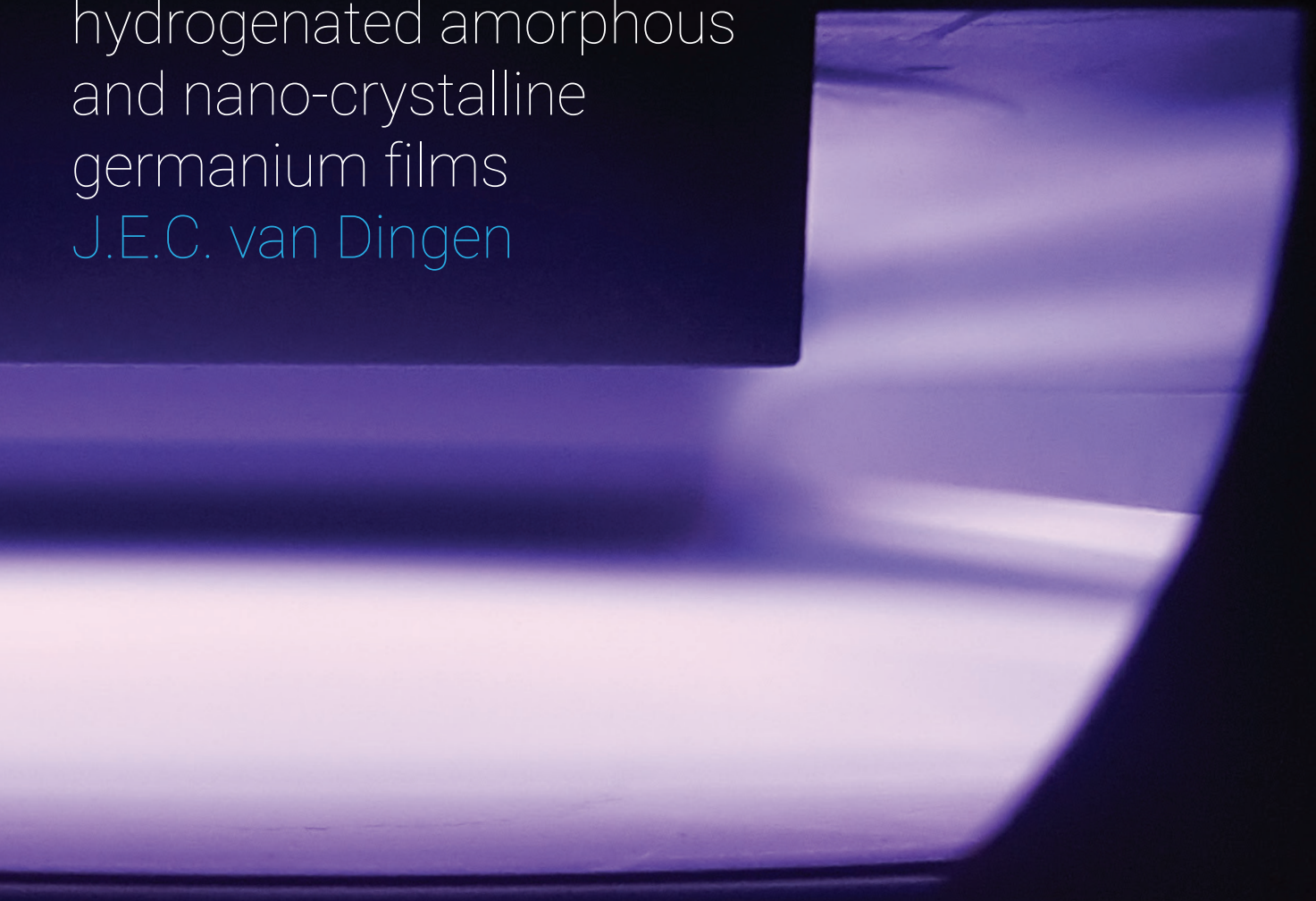

Technische Universiteit Delft

TU Delft

Improving the stability and opto-electrical properties of hydrogenated amorphous and nano-crystalline germanium films

by

J.E.C. van Dingen

to obtain the degree of Master of Science
at the Delft University of Technology,
to be defended publicly on Thursday April 29, 2021 at 14:30 PM.

Student number:	4191293	
Project duration:	March 9, 2020 – April 29, 2021	
Thesis committee:	Prof. dr. A. H. M. Smets,	TU Delft, Professor & Supervisor
	Dr. L. Mazzarella,	TU Delft, Assistant Professor
	Dr. J. Dong,	TU Delft, Assistant Professor
	Ir. T. de Vrijer,	TU Delft, PhD candidate & Daily Supervisor

TU Delft

Acknowledgements

With this thesis project I complete my Master of Science program in Sustainable Energy Technology at Delft University of Technology. I am grateful for having had the opportunity to gain hands-on experience in the interesting field of photovoltaic material development.

First of all, I would like to thank Thierry de Vrijer and Arno Smets for supervising me during these difficult times of the coronavirus pandemic. Thierry guided me as daily supervisor and helped me focus on the fundamentals of my research. He provided structure in the process and gave very helpful feedback. Furthermore, I very much appreciated Arno's enthusiasm, passion for photovoltaic materials and particular interest for this project. He showed that "doing something different" will eventually pay off, which I believe is true for this project.

I would also like to thank my predecessor Bilal Bouazzata for taking the time to explain all the ins and outs of the topic. He was always happy to help me for all kinds of questions about the project. Furthermore, I would like to thank my lab partner Paul Roelandschap, whith whom I worked together on processing and characterizing the Ge:H films. It was helpful to discuss about all aspects related to the project and cooperate with the experimental work. This lab work could also not have been carried out without the assistance of Martijn Tijssen and Daragh O'Connor. Numerous times they worked tirelessly on getting CASCADE operational again after problems occurred with the system.

Lastly, I would like to thank Jacintha for motivating me during this long and challenging process. Also, I would like to thank my mother and family for their unconditional support and patience during my entire studies.

J.E.C. van Dingen
The Hague, April 2021

Abstract

In the far majority of current photovoltaic devices, photons with an energy below 1.1 eV are not utilized. Adding a Plasma Enhanced Chemical Vapor Deposition (PECVD) processed germanium bottom cell to a multi-junction device has the potential to provide a low-cost boost in conversion efficiency by utilizing a part of this spectral range below 1.1 eV.

For this thesis, 89 amorphous/nano-crystalline hydrogenated germanium (a-/nc-Ge:H) films were PECVD processed with the objective of creating a device quality material that is stable, intrinsic and has a high photoresponse. These characteristics are required to enable p-i-n bottom cell integration in a multi-junction device and prevent post-deposition oxidation and carbonation. To this end, the following three approaches were applied: I. Boron doping to increase the activation energy; II. Hydrogen plasma treatment (HPT) to decrease the defect density of the material with hydrogen passivation; III. A decreased electrode gap to improve the photoresponse. These approaches were integrated in the sample preparation steps. Subsequent film characterization was carried out by using vibrational analysis, elemental analysis, and opto-electrical analysis.

The influence of boron doping was considered insignificant and the influence of hydrogen plasma treatment was considered inconclusive. Furthermore, a decreased electrode gap did not result in a higher photoresponse. Reported photo-/dark conductivity ratios (σ_{ph}/σ_{d}) were in the range of 1-7. However, the decreased electrode gap resulted in lower deposition rates and higher refractive indices of 4.9-5.0 (compared to 4.1-4.9 for a 20 mm electrode gap), indicating denser films.

A substantial fraction of the films was processed at an increased temperature of 275 °C. It was found that increasing the processing temperature from 200 °C to 275 °C resulted in considerably denser films with refractive indices of up to 5.2, leading to higher activation energy (up to 314 meV) and very low post-deposition oxidation and carbonation. Therefore, by increasing the processing temperature, it was accomplished to produce denser, more stable films, which have a lower bandgap energy and are more intrinsic.

Contents

List of Figures

1 Introduction

This introduction aims clarify the relevance of this thesis by providing a brief description the research context and motivation. Furthermore, the scope of this research will be considered together with a short overview of the report structure.

1.1. Research context

1.1.1. The need for sustainable energy

To achieve the goal of the Paris Agreement and pursue efforts to limit the average global temperature rise to 1.5 °C above pre-industrial levels, greenhouse gas (GHG) emissions must be reduced to zero by 2050. The agreement entails that the warming should be limited to well below 2 °C and efforts should be taken to limit this increase to 1.5 °C. Failing to comply with the Paris Agreement will have a disastrous impact on human society and the environment we live in [12]. As it is clear that greenhouse gas emissions from burning fossil fuels are responsible for climate change, it is crucial to replace fossil energy sources by sustainable alternatives in the next few decades.

Figure 1.1 shows the total energy supply worldwide from 1800 to 2019. The y-axis indicates the global direct energy consumption in terawatt-hour (TWh). From the figure the following two main trends can be observed:

1. Fossil fuels such as coal, oil and natural gas have been the largest sources of energy since the 1900's and their present day share in the energy mix remains substantial.

2. The total energy consumption shows a large increase over time, especially the period of 1950-2019.

The surge in energy consumption from figure 1.1 is expected to continue in the future as global population grows and energy use per capita is rapidly increasing in developing countries [13]. As a consequence, it becomes clear that action is needed to meet the energy needs of tomorrow while cutting down emissions. In this endeavour, the large scale implementation of photovoltaics (PV) will be of vital importance [14].

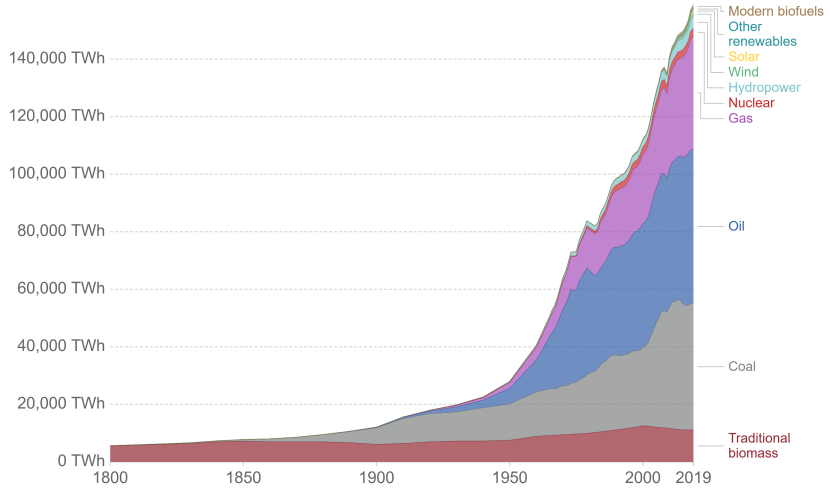

Figure 1.1: Global direct energy consumption 1800-2019 [1] [2].

1.1.2. Photovoltaics as key technology for future energy supply

Photovoltaics will play a crucial role in the energy transition due to persistently declining costs [3], scalability and high abundance of solar radiation in many regions worldwide. It has to be noted however that energy from photovoltaics is not completely free of greenhouse gas emissions, as carbon dioxide is released during fabrication processes. Nonetheless, these emissions per unit of energy produced are much lower than fossil fuel emissions [15].

To learn why photovoltaic technology has a large growth potential, the price trend for solar modules will be considered. Figure 1.2 shows the effect of upscaling on the module price: the more modules manufactured, the lower the price. This relation demonstrates that the inflation adjusted price has decreased exponentially over the period of 1980-2019, for which an exponential increase of cumulative production was accomplished. For each doubling in cumulative production, the price went down by 25 % [3]. In 2019, a cumulative production of 600 GWp (gigawatt-peak) at a price of 0.15 €/Wp (Watt-peak) was established (data point closest to lower-right corner of the graph) [3]. This is a considerably large cumulative production at already a quite low price. Further upscaling is needed to continue this trend, resulting in even lower costs and TWp (terawatt-peak) production levels. In this upscaling process, research can help to improve PV efficiencies and use resources more effectively.

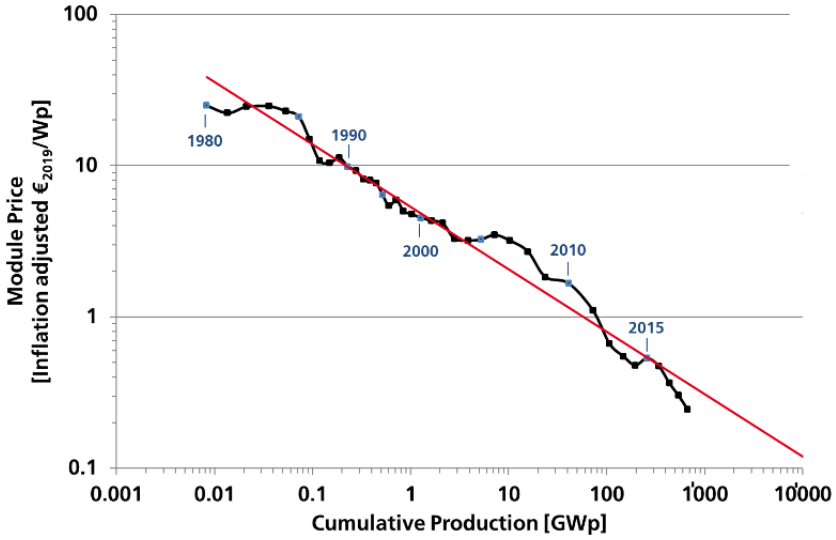

Figure 1.2: Price learning curve of photovoltaic modules [3]

1.2. Research motivation

1.2.1. Low-cost multi-junction PV as next step in solar energy revolution

Development of a low-cost multi-junction photovoltaic device could serve as the next step in the solar energy revolution. To understand why, the working principles of a multi-junction photovoltaic device should first be examined in more detail. A multi-junction has, when compared to a single junction, the benefit that a broader range of photon energies can effectively be used to generate charge carriers.

For a single junction device, only photons with bandgap energy or higher can generate charge carriers. All charge carriers that are generated by these photons have an energy equal to the bandgap. This has the consequence that a significant fraction of energy is lost due to thermalization and non-absorption. In case of thermalization, the photon energy is larger than the bandgap. The excess photon energy cannot be used and is dissipated as heat. Non-absorption happens when photons have an energy that is lower than the bandgap. These photons are not able to generate charge carriers and are transmitted through the material, thereby not contributing to the energy conversion process.

For a multi-junction device on the other hand, these thermalization and non-absorption losses are reduced by stacking multiple subcells according to their respective bandgap energy to cover a broad spectral range. In the multi-junction device, the photons reach the layer with the highest bandgap first, so that the high photon energies can effectively be used. The next layer that transmitted photons reach is the layer with the second largest bandgap, and so on. This way, the solar spectrum can be used more efficiently. In figure 1.3, the spectral utilization of a multi-junction device is visualized.

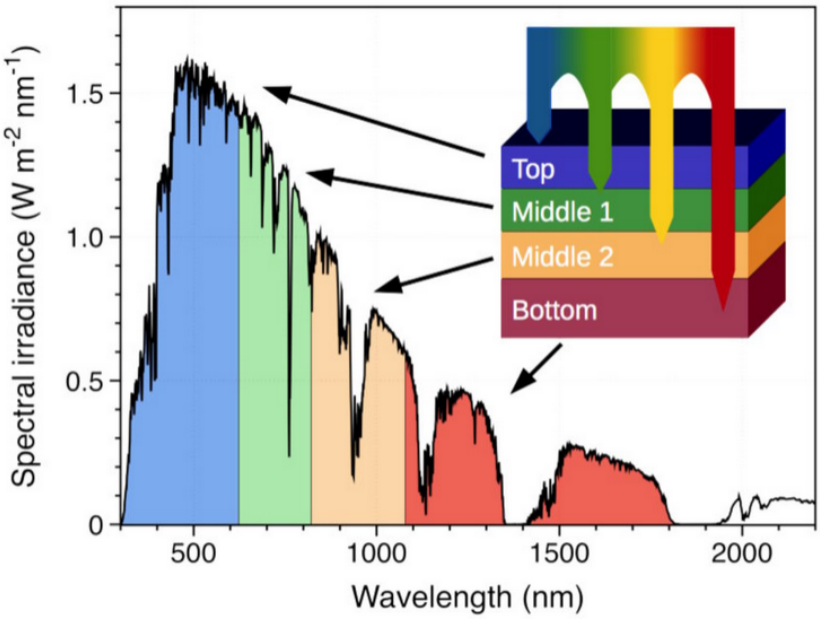

Figure 1.3: Spectral utilization of a multi-junction device [4]

Now that the general working principle of a multi-junction is briefly explained, a short discussion about the costs of these devices will follow. Multi-junction solar cells are generally more expensive than single junctions as extra processing steps are involved and typically more expensive materials are used. However, in many cases multi-junctions can be made very thin due to high absorption. The layers of thin (film) solar cells are several hundreds of nanometers thick, requiring much less material than thicker wafer based cells with a thickness of several hundred micrometers. As discussed earlier, multi-junctions are generally more expensive than single junctions. If the price of these multi-junctions can be successfully brought down, by for instance using cheaper processing techniques, multi-junctions can become a low-cost technology that is very efficient and suitable for large scale applications.

1.2.2. Thin film germanium as candidate for bottom cell

In this thesis, a RF-PECVD processed hydrogenated germanium film (Ge:H) is investigated as low-cost candidate for a multi-junction bottom cell. RF-PECVD or radio frequency plasma enhanced chemical vapour deposition can be described as relative low temperature method to deposit a material on a substrate using a plasma. Due to the relative low temperature of RF-PECVD at around 200-300 °C, this is a relatively cheap processing technique.

The use of germanium as bottom cell of a multi-junction can be justified by comparing the bandgap of germanium with the materials that can be used for the higher junctions. Germanium is a group IV semiconductor and crystalline germanium has a bandgap of 0.67 eV. For a thin film multi-junction device, nanocrystalline silicon with a bandgap of 1.1-1.3 eV is typically used as bottom cell. This means that all photons with energies lower than 1.1-1.3 eV are not absorbed. By introducing a low bandgap germanium junction, the spectral band of 0.67-1.1 eV can be utilized, enabling a open voltage increase of 0.2-0.4V. Figure 1.4 presents an overview of group IV semiconductors with their corresponding bandgap and spectral utilization, including an amorphous germanium layer. A great advantage of using a low bandgap bottom cell is that it will never be a current limiting factor since a large number of photons are present in the infrared part of the spectrum. The bottom junction will also not limit the fill factor (FF) in this case, because the high photon flux in the range of 0.67-1.1 eV can generate a high current density. Therefore, a relatively high defect density is allowed for this type of bottom cell.

alloy	Band gap (eV)
a-Ge:H	0.6-1.0
c-Si	1.1
nc-Si:H	1.1-1.3
a-SiGe:H	1.4-1.6
a-Si:H	1.6-1.8
a-SiOx:H	>2.0

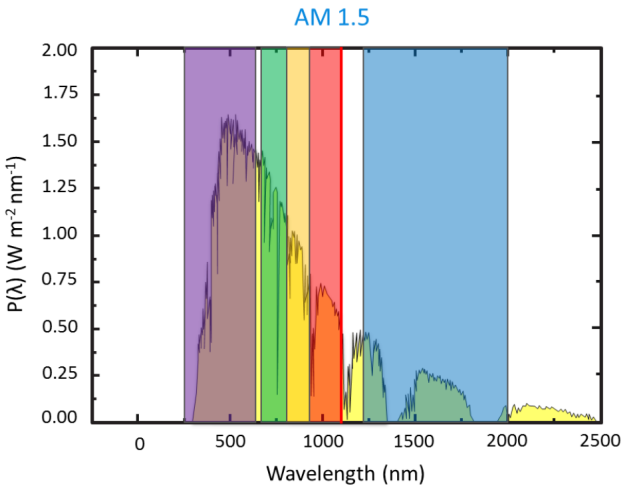

Figure 1.4: Spectral utilization of group IV multi-junction solar cell [5].

1.2.3. Integration in photoelectrochemical cell

To effectively deal with the intermittent nature of solar power, a direct solar to fuel conversion (STF) step can be advantageous. A multi-junction and electrochemical cell can be combined in a photoelectrochemical cell (PEC) to directly convert solar energy into chemical energy. This chemical energy in the form of a fuel can then be stored or transported. This thesis is part of a larger research project named DISCO (DIrect Solar to CO conversion), which has the aim to develop such a photoelectrochemical cell for the direct conversion of sunlight, water and carbon dioxide into a syngas. This syngas consists of mainly hydrogen and carbon monoxide. The DISCO project focuses on making the device with non-toxic and earth abundant elements.

Adding a germanium based bottom cell to a photoelectrochemical cell has the benefit that the solar spectrum below the silicon bandgap is used as well, resulting in larger STF conversion efficiencies and potential higher control of product selectivity due to the ability of generating a higher voltage.

1.3. Research scope

1.3.1. Aim

The aim of this research is to develop a device quality plasma enhanced chemical vapor deposition (PECVD) processed hydrogenated germanium (Ge:H) film. Adding a PECVD processed germanium bottom cell to a multi-junction device can facilitate a low-cost boost in conversion efficiency by using the additional spectral range of 0.67-1.12 V.

1.3.2. Problem statement

The following four substantial issues for PECVD processed Ge:H films have been reported that impede the development of a device quality material:

- High defect density, indicated by a relatively high dark conductivity (σ_d) of in some cases up to 0.2 $(\Omega \cdot cm)^{-1}$ [8, 16, 17];
- Relatively low activation energies [18] (E_{act}) of 20-260 meV [8, 16, 17];
- A poor photoresponse [19], indicated by a photo-/dark conductivity ratio (σ_{ph}/σ_d) of 1-6 [8, 16, 17];
- Post-deposition oxidation, indicated by the substantial presence of germanium-oxygen (GeO_x) complexes for Ge:H films a with relatively low refractive index ($n_{@600nm}$) [8, 16, 17].

These issues all have a very close connection to each other as they are directly related to the defect states in the material. For amorphous germanium, the high defect density and low E_{act} of 150-250 meV can be associated with a dominant defect type that has energy levels close to the conduction band edge [8, 18]. Moreover, the high defect density of the reported films is related to the high dark conductivity and corresponding poor photoresponse. Lastly, GeO_x complexes originating from post-deposition oxidation were deemed to be responsible for passivating this dominant defect type and introducing a smaller defect density very close to the conduction band with E_{act} of 50-75 meV [8].

These issues are problematic for several reasons. Firstly, the material needs to be intrinsic for the construction of a p-i-n junction, a configuration that is favorable for this type of thin film photovoltaics. In this p-i-n configuration, an intrinsic absorber layer is sandwiched between a p-type and n-type layer. For the i-layer, the Fermi-level has to be positioned exactly halfway of the conduction and valence band with an activation energy (E_{act}) half of the bandgap energy. The Ge:H films that were reported in earlier research are far from intrinsic as they have a relatively low E_{act} of 20-260 meV, which is significantly less than half the electrical bandgap energy of roughly 1 eV. Secondly, a high defect density will cause increased recombination, resulting in a decreased photovoltaic performance of the material. Furthermore, post-deposition oxidation is problematic as it strongly affects the material structure and opto-electrical properties, as is demonstrated for example by a significant E_{act} decrease. Lastly, the material needs to have a high photoresponse to facilitate a sufficient current density as bottom cell of a monolithically integrated 2-terminal multi-junction device.

1.3.3. Approach

Three approaches were investigated to overcome the previously discussed issues:

I Boron doping to increase E_{act}, thereby obtaining a more intrinsic Ge:H film.

II Hydrogen plasma treatment (HPT) to decrease the defect density of the material by hydrogen passivation.

III A decreased electrode gap to improve the photoresponse.

These approaches were integrated in the sample preparation steps. After the preparation steps, opto-electrical characterization was carried out by the following methods: Fourier transform infrared spectroscopy, spectroscopic ellipsometry, raman spectroscopy, energy dispersive x-ray spectroscopy, photoconductivity measurements and dark conductivity measurements.

1.4. Report structure

The report has the following structure. Chapter 2 provides theoretical background for thin film solar cells. Processing methods are discussed in chapter 3. The used characterization methods will be explained in chapter 4. The experimental results can be found in chapter 5. Finally, chapter 6 presents the conclusion and recommendations.

2

Theoretical background

This chapter provides the theoretical background with fundamental principles for (thin film) solar cells such as the solar spectrum, electronic band structure and the photovoltaic effect. Also some general germanium characteristics will be discussed.

2.1. Solar radiation

A closer look at solar radiation will be taken to understand how photovoltaic technology can capture and convert visible sunlight and other radiation into electrical energy. Nuclear fusion processes in the sun cause the surface temperature to reach about 5800K [20]. As a result, the sun emits electromagnetic radiation with a spectrum that stretches from deep ultraviolet to far infrared [6]. The wavelength of the electromagnetic waves are related to its frequency and the speed of light through the following expression:

$$c = \nu\lambda, \tag{2.1}$$

where c is the speed of light, ν the frequency and λ the wavelength of the electromagnetic waves. In this formula, light is clearly considered to behave as an electromagnetic wave. However, due to the wave-particle duality of light, it can also be seen as a particle, or photon, where each photon carries a discrete bundle of energy. In this case, the photon energy is dependent on the frequency of its wave according to the relation:

$$E = h\nu, \tag{2.2}$$

where E is photon energy, h is Planck's constant and ν is the frequency of the corresponding electromagnetic wave.

When solar radiation passes through the atmosphere, it is attenuated by atmospheric gases and particles that cause scattering and absorption; the more atmosphere through which the sunlight passes, the larger the attenuation. The relative distance that the sunlight travels through the atmosphere is expressed with a so called air mass coefficient. The air mass coefficient defines the ratio between the direct optical path length through the earth's atmosphere and the atmospheric path length normal to the earth's surface at sea level. Air mass 1.5 (AM1.5) is the standardized atmospheric path length and is used for characterization of terrestrial solar panels. The reason for using an air mass coefficient that is larger than one has to do with the fact that solar panels do not generally operate under exactly one atmospheric thickness. If the sun is visible at an angle between the zenith and horizon, the effective atmospheric thickness will be larger than one, which is typically the case for many of the world's major population centres that lie in temperate latitudes. AM1.5 represents the atmospheric thickness at mid-latitudes and corresponds to a solar zenith angle of 48.2°. The intensity of AM1.5 is normalized at 1000 W/m^2 [21]. In figure 2.1 the AM1.5 spectrum is shown together with the AM0 and 6000 K blackbody radiation spectrum.

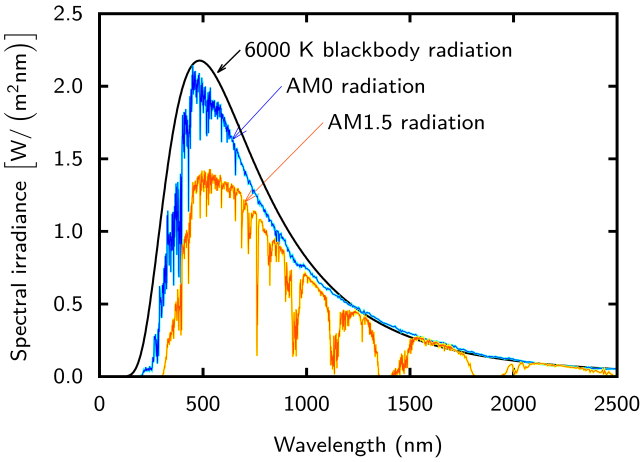

Figure 2.1: AM0 spectrum, AM1.5 spectrum and 6000 K blackbody radiation spectrum [6]

2.2. Germanium characteristics

Since this research investigates the development of a thin film germanium layer, it is useful to have a general understanding of germanium and its characteristics. Germanium is a lustrous, hard-brittle, grayish metalloid, having properties of both metals and nonmetals. The bandgap of germanium in its crystalline form is 0.67eV [7]. Furthermore, the position of germanium in the periodic table of elements is in group 14. Semiconductor elements from this group, such as germanium and silicon, are referred to as group IV semiconductors, meaning that they have 4 valence electrons. The position of germanium in the periodic table entails that it is chemically similar to its group neighbours silicon and tin. Germanium is considered as an essentially non toxic element [22][23].

The abundance of germanium in the earth crust is 1.6 parts per million by weight [23]. Some more known elements such as tin and zinc have an abundance of 2.3 and 70 ppm respectively. Like silicon, germanium naturally reacts and forms complexes with oxygen, therefore it does not occur in its pure form in nature. Today, germanium is mined primarily from sphalerite (the primary ore of zinc), though germanium is also recovered commercially from silver, lead, and copper ores[23]. Its cost range from 120-360$ per 100 gram, depending on its purity [24].

2.3. Fundamental semiconductor principles

2.3.1. Atomic structure

Understanding the atomic structure of semiconductors is essential, as atom bonds and lattice arrangement determine the electrical and optical behavior of a material. Group IV semiconductors, such as germanium and silicon, have four valence electrons. This entails that each atom can covalently bond with four neighboring atoms. When multiple atoms form bonds, a network is developed. In this network, the atoms can be connected in an ordered pattern or in a disordered way.

In a crystal, the atoms are arranged at equal spacing and bonding angle. This type of bonding coordination is called tetrahedral four-fold or diamond cubic. When there's no pattern in the bonding arrangement on a larger scale, the material is referred to as amorphous. The atomic structure of amorphous material is described as a continuous random network. If a consists of crystalline grains in a hydrogenated amorphous tissue, it is referred to as nano-crystalline.

Figure 2.2 shows the atomic structure of (a) crystalline silicon in a ordered lattice and (b) amorphous silicon with a continuous random network. In the crystalline material, where all the atoms have equal spacing and bonding angle, four covalent bonds with their neighbors are formed for all atoms. In the amorphous network on the other hand, not all atoms form four bonds, as can be seen in the figure. In a three-fold coordination there is one valence electron

that does not form a covalent bond. This valence electron that does not form a covalent bond is referred to as a dangling bond, which is known to introduce electronic states within the band gap [7].

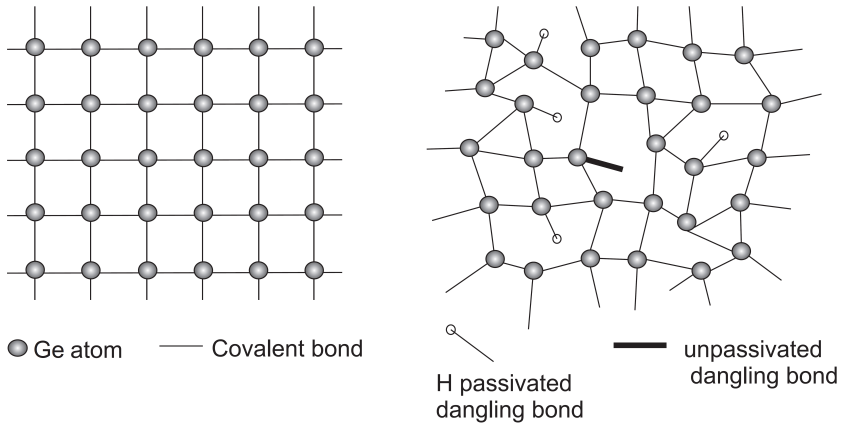

Figure 2.2: Atomic structure of: c-Ge (left), a-Ge:H (right). Modified from [7].

The method of deposition plays an important role in how the atoms form bonds and develop structure. In chapter 3, plasma enhanced chemical vapour deposition will be discussed as method for making a-Ge:H (hydrogenated amorphous germanium) and nc-Ge:H (hydrogenated nanocrystalline germanium). A hydrogenated nanocrystalline material, also referred to as microcrystalline material, consists of small grains with a crystal lattice that are embedded in a hydrogenated amorphous tissue [6].

2.3.2. Density of States and electronic band structure

The concept of density of states (DOS) is essential to understand the opto-electrical characteristics of a semiconductor. The density of states function describes the number of allowed electronic states for a system with a certain volume and energy. For a perfect crystalline semiconductor material, the density of states is zero in the electrical bandgap. Within this bandgap, no electronic states can exist. The collection of energy states above the bandgap corresponds to the conduction band and the collection of energy states below the bandgap corresponds to the valence band. When the material is not perfectly crystalline, so called localized states within the bandgap can be present [25]. These localized states can occur close to the band edges or around the center of the bandgap and are the result of defects in the material.

The average energy of electrons in a material is represented by the Fermi energy, or Fermi level. The Fermi level of a perfect crystalline material with no impurities lies in the middle of the bandgap. In this case, the material is referred to as intrinsic.

2.3.3. Doping

The Fermi level of a material can be manipulated by introducing doping atoms, which can accept or donate electrons to the surrounding material. In case the doping atoms are added to a group IV semiconductor material, acceptor atoms have three valence electrons and donor atoms have five valence electrons.

The most used atoms for doping are boron (B) and phosphorous (P), which can be used as electron acceptor and donor respectively. These doping atoms are used to create p- and n-type material, needed to create a p-n junction that can separate charge carriers. N-type material has a Fermi level close to the conduction band and is made by introducing electron donor atoms. P-type material has a Fermi level close to the valence band and is created by introducing electron acceptor atoms. Figure 2.3 shows the band diagrams of intrinsic material, n-type material doped with electron donors and p-type material doped with electron acceptors.

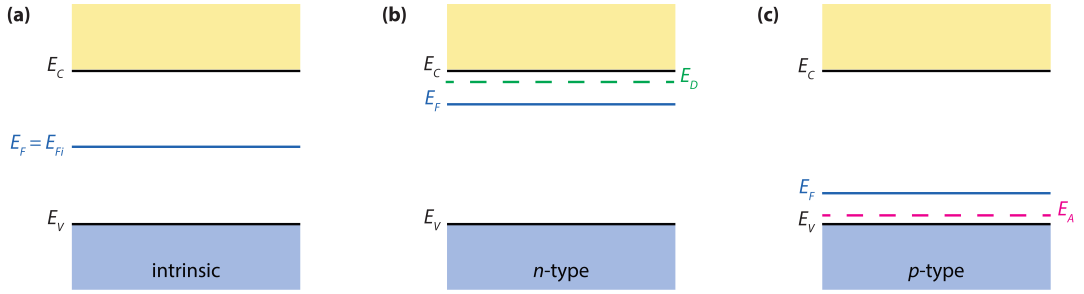

Figure 2.3: (a) intrinsic semiconductor, (b) n-type material doped with electron donors, (c) p-type material doped with electron acceptors [6].

2.3.4. Direct and indirect bandgap materials

While the long range order between amorphous and crystalline silicon is completely different, they still share very similar short range order, resulting in similar energy state band configurations. One important difference is that crystalline silicon behaves as a direct bandgap material, whereas amorphous silicon behaves as an indirect bandgap material. In an indirect bandgap material, not only energy transfer from photon to electron has to take place but also momentum has to be transferred from the lattice to excite the electron from the valence to the conduction band. It has to be noted that crystalline silicon has both a direct and an indirect transition in the band diagram. However, the direct transition (3.4eV) is much larger compared to the indirect transition (1.12eV).

In an amorphous material the atomic network is not periodic, resulting in loss of distinction between a direct and indirect bandgap [7]. Because of this effect, amorphous silicon behaves like a direct bandgap material.

2.4. The working principle of a solar cell

Solar cells can convert solar radiation into electric energy by using the photovoltaic effect. The photovoltaic effect is the generation of voltage and electric current in a material upon exposure to electromagnetic radiation. The absorbed radiation causes the excitation of an electron to a higher energy state; energy is transferred from the absorbed radiation to the excited electron. When an electron is excited to a higher energy level, it jumps across a bandgap from the valence band to the conduction band. This implies that for an ideal semiconductor only photons with an energy of at least the bandgap energy can cause an electron to be excited from valence to conduction band; photons with an energy smaller than the electrical bandgap, E_G, will not be absorbed but will traverse the material without interaction.

When an electron is excited, it leaves behind a void, called a hole. This hole behaves like a particle with a positive elementary charge. Both electrons and holes are so called charge carriers and can move through the material.

In a photovoltaic device, an electric potential and current can only be established when the following consecutive processes occur:

(i) an electron is excited from the valence band to the conduction band, resulting in the creation of an electron-hole pair;

(ii) charge carriers of the generated electrons-hole pairs are separated;

(iii) electrons and holes are separately collected at the terminals of the device.

Process (i) has been discussed previously in this section. Processes (ii) and (iii) will now be explained. After excitation of an electron, separation of the electrons and holes is required to use the energy stored in the electron-hole pair. When the electron-hole pair is not separated after its creation, it will typically recombine after a short moment; the electron falls back to its initial energy level in the valence band. Separation of the electrons and holes in solar cells is most commonly facilitated by a so called p-n junction. A p-n junction facilitates the separation of charge carriers by the electric field that is formed in the junction. The p-n

junction is characterized by a very thin boundary region between n-type and p-type material that is depleted of mobile charge carriers and therefore has an electric field, see figure 2.4. Minority charge carriers -electrons in p-type material or holes in n-type material- that are generated by absorption of photons can diffuse to the space charge region and are then pushed by the electric field to the opposite side of the space charge region. This way the p-n junction separates the generated charge carriers with its electric field.

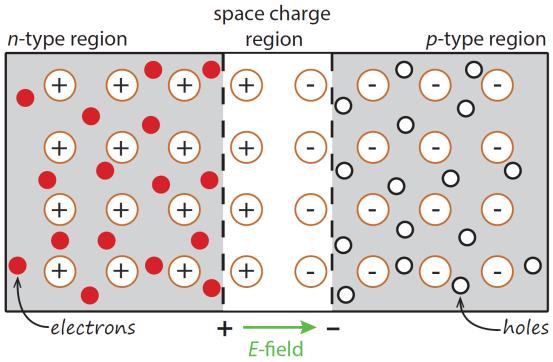

Figure 2.4: p-n junction [6]

Finally, when the charge carriers are separated, they can be extracted from the semiconductor material at electrical contacts so that they can flow through a connected circuit. Only electrons, not holes, can be present in the connected circuit.

Important loss mechanisms for solar cells are thermalization and non-absorption losses. Thermalization takes place when photons exceed the bandgap energy and non-absorption occurs when photons have below bandgap energy. By stacking materials with different bandgaps in a so called multi-junction, these losses can be reduced drastically.

2.5. Light absorption in photovoltaic materials

As light travels through an absorptive medium, it will be absorbed according to the following relation

$$I(x) = I(0)e^{-\alpha x} \tag{2.3}$$

where I(x) is the light intensity (Wm^{-2}) after a distance x (cm) is traveled, I(0) is the intensity before the light has entered the medium, α is the absorption coefficient for a certain wavelength (cm^{-1}). The absorption coefficient depends on the material and the wavelength. Figure 2.5 shows this relation for different semiconductors materials. It can be observed that germanium has a relative high absorption coefficient for a wide range of wavelengths. Gallium Arsenide (GaAs) and Indium Phosphide (InP) show a clear drop or ”knee” in their absorption coefficient at wavelenths of 800 and around 900 nm respectively. This knee is a characteristic for direct bandgap materials. Silicon is known to have a direct and indirect bandgap at 3.5 eV (350 nm) and 1.1 eV (1100 nm) respectively, which can be observed as a steep drop at around 350 nm and a more dull knee at around 1100 nm.

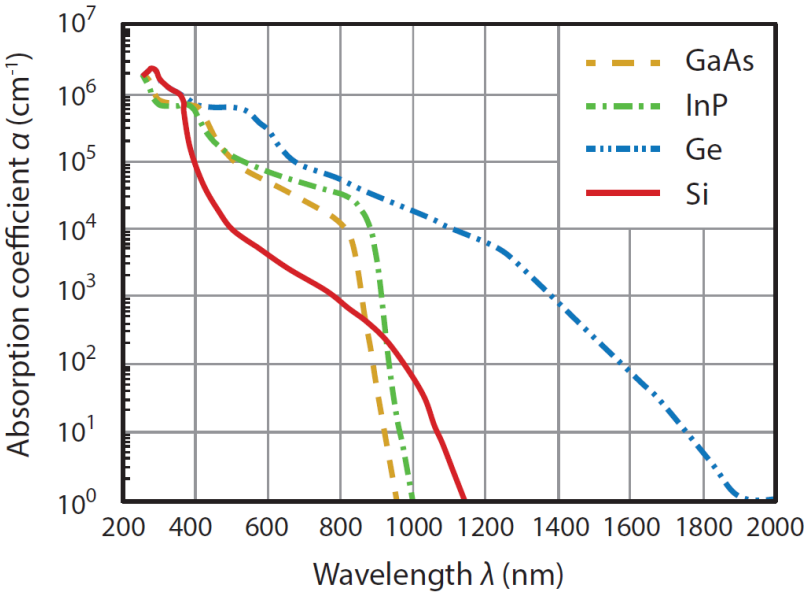

Figure 2.5: The absorption coefficient α cm^{-1} for different semiconductor materials [6].

2.6. Hydrogenated germanium films

2.6.1. p-i-n junction

For defect rich thin film photovoltaic materials, such as a PECVD processed Ge:H film, a p-n junction is not effective due to the strongly decreased diffusion length for charge carriers. In this case, a p-i-n junction can be constructed. In this configuration, the n-type and p-type layer are made very thin because of this short diffusion length. Between the p-type and n-type layer, a thicker intrinsic layer is placed to function as absorber layer. Across this intrinsic layer an electric field is formed by the n- and p-type layer. In such a device, electronic drift is the main transport mechanism. This is in contrast with a p-n junction where diffusion is the main transport mechanism. Figure 2.6, shows the band diagram of a p-i-n junction.

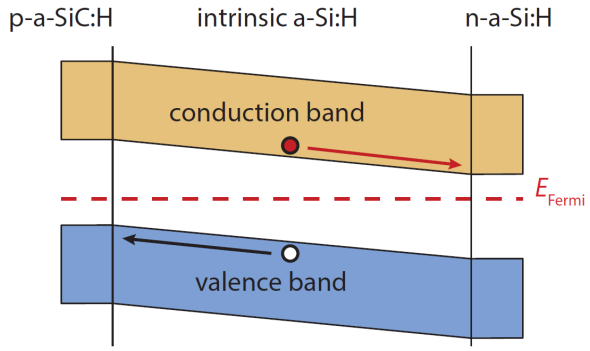

Figure 2.6: Band diagram of a p-i-n junction [6].

2.6.2. Influence of post-deposition oxidation

Earlier research on plasma enhanced chemical vapor deposition processed hydrogenated germanium (PEVCD Ge:H) films showed that post-deposition oxidation strongly degrades the film quality [8, 16, 17]. GeO_x complexes associated with this post-deposition process, were absent for films with a relatively high refractive index ($n_{@600nm}$) of roughly 4.8 or above. This $n_{@600nm}$, determined for the wavelength of 600 nm, is thought to be an adequate indicator for the void density and porosity of the material, where low $n_{@600nm}$ signifies a porous Ge:H network. The observed absence of GeO_x complexes for high $n_{@600nm}$ was attributed to the

inability of water vapor to penetrate a dense Ge:H film.

The influence of post-deposition oxidation on the activation energy (E_{act}) and defect states is visualized by figure 2.7. E_V, E_G and E_C indicate the valence energy level, electrical bandgap and conduction energy level respectively. The figure visualizes that oxidation results in the passivation of the dominant defect type and that a smaller defect density very close to the conduction band is introduced, resulting in an E_{act} decrease.

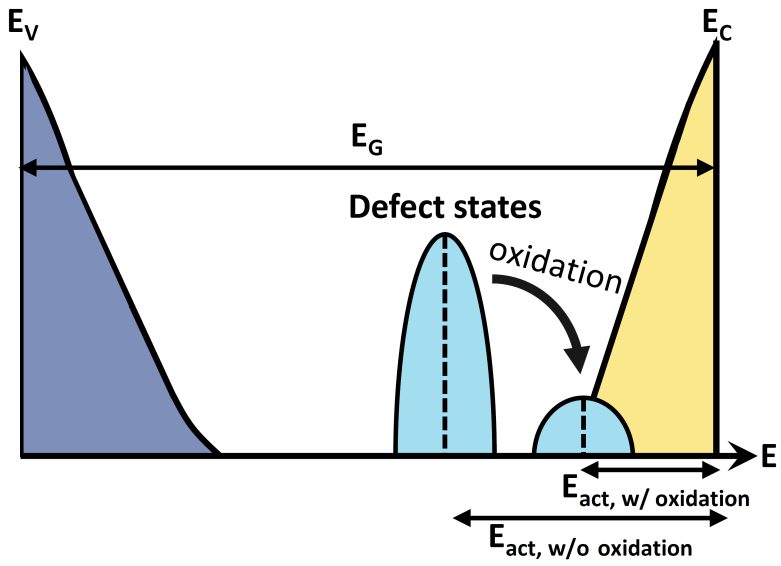

Figure 2.7: Density of states diagram for a hydrogenated germanium material, demonstrating the effect of oxidation on the defect density and E_{act} [8].

3

Sample preparation

This chapter provides the procedure that is used for processing the hydrogenated germanium film (Ge:H) on glass and mono-crystalline silicon. The first step of the procedure was cleaning the glass and silicon substrate. The next step was Ge:H deposition on the substrate using radio frequency plasma enhanced chemical vapor deposition (RF-PECVD). After processing the germanium film, aluminium contacts were deposited on the sample for electrical characterization. Finally, an annealing step was applied to enhance the bonding of the electrical contacts to the germanium film and reduce surface traps at the metal semiconductor interface. Figure 3.1 gives an overview of the sample preparation.

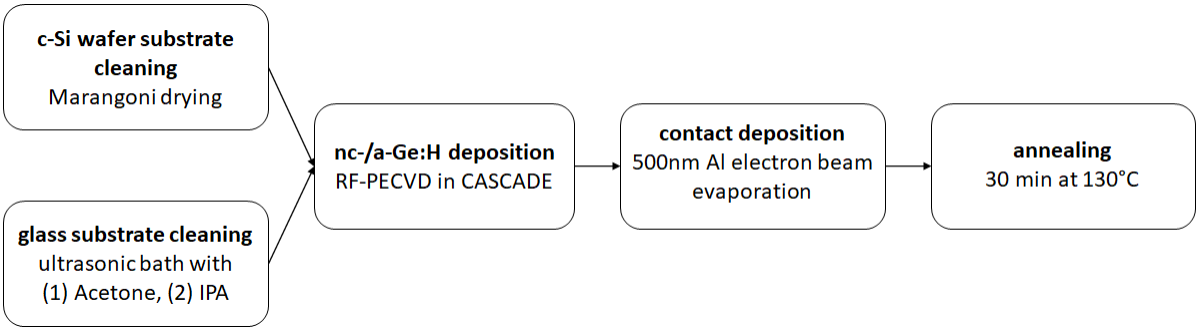

Figure 3.1: Sample preparation procedure for wafer and glass substrates.

3.1. Substrate cleaning

Two types of substrates were used for Ge:H deposition: 10 cm x 2.5 cm Corning Eagle XG glass and Siegert 100 mm diameter mono-crystalline silicon wafers with a thickness of 525 µm. The cleaning method for the two types of substrate will be discussed below.

For the wafer substrate, the surface oxide layer on the c-Si wafer was removed by etching with a 0.5 % HF solution. After that, the wafers were rinsed with water and IPA and then dried using the Marangoni effect to effectively remove residual particles on the surface. Subsequently, the wafers were cut into quarters to reduce material use and leave space for a glass substrate to fit on the 10 cm x 10 cm substrate holder of CASCADE.

To obtain suitable glass substrates for processing in CASCADE, 10 cm x 10 cm Corning Eagle XG glass was cut into four rectangular pieces with a glass cutting tool. Particles on the glass surface were removed by putting it in an ultrasonic cleaning bath for a total time of 20 minutes, of which 10 minutes in acetone and then another 10 minutes in isopropyl alcohol (IPA).

3.2. Plasma enhanced chemical vapour deposition

The germanium film was deposited on a substrate by radio frequency plasma enhanced chemical vapour deposition (RF-PECVD), which allows for deposition of thin films at relatively low temperatures of 200-300 °C. The PECVD processing has been performed with the CASCADE reactor unit that is located in the CR10,000 (clean room class 10,000) area of the Else Kooi Laboratory in Delft. CASCADE is the abbreviation of Cascaded Arc Solar Cell Apparatus Delft Eindhoven. Figure 3.2 shows a schematic overview of the PECVD setup.

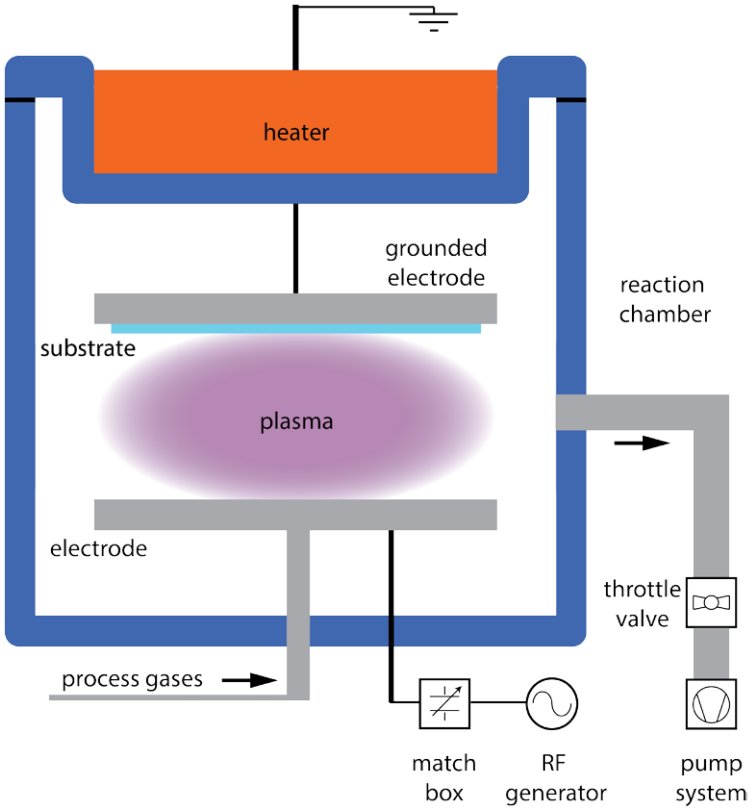

Figure 3.2: Plasma Enhanced Chemical Vapor Deposition (PECVD) setup, adapted from [9].

For the PECVD process, the precursor gases germane (GH_4) and hydrogen (H_2) were introduced in a reaction chamber by laminar flow and subjected to an oscillating electric field, ionizing the precursor gases and causing a visible glow discharge. A glow discharge is a plasma formed by the passage of electric current through a gas. The plasma consists of reactive radicals, ions, neutral atoms, molecules and electrons. Dissociation and ionization are two processes that take place in the plasma and lead to the formation of highly reactive free radicals that attach to the substrate, resulting in the growth of the thin film. The plasma was formed between two circular electrodes with a diameter of 160 mm. A radio-frequency generator connected to the bottom electrode was responsible for establishing the electric field. The substrate holder was placed directly below the grounded top electrode. The electrode gap between the top and bottom electrode could be modified by the setting the height of the circular bottom electrode, that was connected to the RF generator. In table 3.1, an overview is presented with the varied processing parameters. A H_2 precursor gas flow ($F(H_2)$) of 200 sccm was used in combination with a GeH_4 gas flow ($F(GeH_4)$) of 0.5-2 sccm, resulting in $F(H_2)/F(GeH_4)$ of 200-400. Furthermore, the indicated values for RF-power, pressure, processing temperature T_S and electrode gap were applied.

Table 3.1: Applied PECVD processing parameters

Deposition Parameter	Range	Unit
$F(H_2)/F(GeH_4)$	200-300-400	-
Power	2.5-5-10	W
Pressure	1-2-3-4-5-6	mbar
T_S	200-275	°C
Electrode gap	11.5	mm

3.2.1. Germanium film growth processes

In this paragraph the processes responsible for the germanium film growth will be considered. Before material can be deposited on the substrate, the precursor gas molecules GH_4 and H_2 have to be broken up into smaller pieces, that can subsequently act as building blocks for the material. The precursor gas molecules GH_4 and H_2 are energetically stable, so energy is needed to break the bonds between atoms. This energy is provided by the free electrons that move from the cathode in direction of the anode. These free electrons cause the atom bonds to break by ionization and dissociation reactions, thereby generating free radicals. These free radicals have an unpaired valence electron, making the particles highly reactive. When using GH_4 and H_2 as precursors, the radical creating reactions that have been identified are [26]:

$$e^- + GeH_4 \rightleftharpoons GeH_3 + H^+ \tag{3.1}$$

$$e^- + GeH_3 \rightleftharpoons GeH_2 + H^+ \tag{3.2}$$

$$H^+ + GeH_4 \rightleftharpoons GeH_3 + H^+ \tag{3.3}$$

Figure 3.3 shows a simplified visualization of the interaction of free radicals with the Ge:H surface, creating a vacancy for Ge bonding, ultimately enabling film growth.

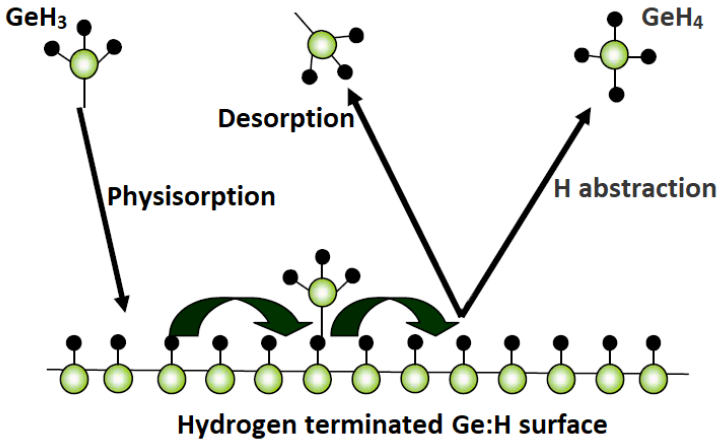

Figure 3.3: Visualization of interaction of free radicals with a-Ge:H surface. Figure adapted from Fig. 5.6 in [27].

3.3. Boron doping

To a subset of samples, boron doping was applied with the aim of increasing E_{act}. In earlier research on a-Ge:H films, boron doping resulted in a shift of Fermi level from close to the conduction band towards midgap [28].

Boron doping in this work was carried out by exposing boron doped films to the plasma during the Ge:H film deposition. Additionally, a selection of these samples was exposed to a pure hydrogen plasma for 5 min before the Ge:H deposition was started, to assimilate boron in the plasma.

3.4. Hydrogen plasma treatment

Hydrogen plasma treatment (HPT) is a method to decrease the defect density by hydrogen passivation. For Ge:H films this method has been applied with RF-glow discharge by F.H. Karg et al. [29]. HPT is also used for hydrogenation of dangling bonds in amorphous and crystalline silicon [30, 31]. In this work, HPT was applied directly after the Ge:H film deposition by exposing the sample to a pure hydrogen plasma for a varying duration of 2-10 min and power of 1.5-20 W.

3.5. Electrical contact deposition and annealing

Parallel rectangular aluminium bars with a thickness of 500nm were deposited in pairs on the germanium film to function as contacts for electrical characterization. The contacts were deposited in Provac PRO 500 under high vacuum conditions, using electron beam evaporation as deposition method. Figure 3.4 shows the working principle of electron beam evaporation. Free electrons are first generated by a filament. A magnetic field then directs the electrons to a aluminium source in a crucible, causing evaporation of the metal. The evaporated aluminium subsequently precipitates on the substrate. A contact mask attached to the substrate is used to delineate contact bars with a size of 20 mm x 1.5 mm, having a parallel spacing of 0.5 mm between paired contacts.

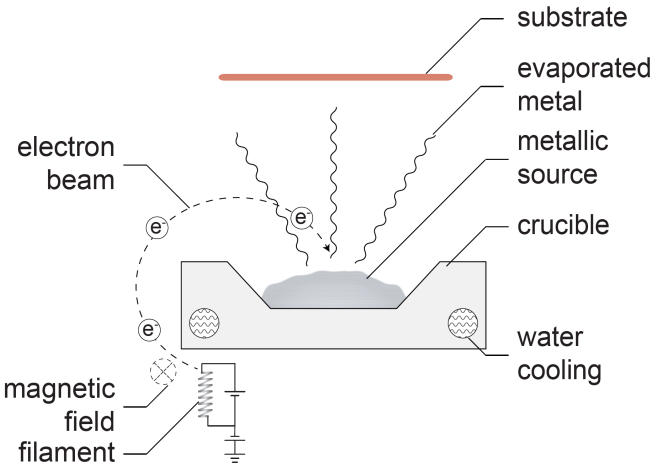

Figure 3.4: Electrical contact deposition by electron beam evaporation [10]

After contact deposition, an annealing step was applied as final step of the sample preparation. This step was carried out to enhance the adhesion of the electrical contacts to the germanium film and reduce surface traps at the metal semiconductor interface. The annealing was carried out at a temperature of 130 °C in a Heratherm Thermo Scientific oven.

4

Characterization methods

To characterize the deposited layer, the following methods were used: Fourier transform infrared spectroscopy, Raman spectroscopy, spectroscopic ellipsometry, dark conductivity measurements, photo conductivity measurements and energy-dispersive x-ray spectroscopy. The films with wafer substrate were used for Fourier transform infrared spectroscopy and energy-dispersive x-ray spectroscopy measurements. The films with glass substrate were used for the Raman spectroscopy, spectroscopic ellipsometry, photoconductivity and dark conductivity.

4.1. Fourier transform infrared spectroscopy

Fourier-transform infrared spectroscopy (FTIR) is a technique used to obtain an infrared absorption spectrum, in which absorption peaks of certain atomic bonds can be detected. For this thesis, FTIR was used to identify and quantify particular bond configurations of the Ge:H film. The FTIR transmission spectrum of the processed quarter wafer samples was measured for a range of 400 cm^{-1} to 4000 cm^{-1} with a Thermo Fisher Nicolet 5700 spectrometer. The acquired transmission spectrum could be transformed into an absorption spectrum with the following relation:

$$A = 2 - \log_{10}(T) \tag{4.1}$$

In this equation, A is the absorbance (-) and T is the transmittance (%). This transformation is necessary to quantify the abundance of particular atomic bonds in the sample.

In figure 4.1 a FTIR absorption spectrum of a typical oxidated Ge:H film is shown. It can be seen that in the wavenumber range of 700-1000 cm^{-1} a substantial peak-structure is present, consisting of many gaussians. The wavelengths in this range are associated with various GeC_x [32, 33] and GeO_x bonds [8]. Other Gaussians in the graph are associated with GeH, SiO_x and SiH [34].

The following procedure was used to quantify the abundance of certain bonds, such as GeH, GeO_x and GeC_x. Absorption peaks were first separated from the background signal by subtracting a manually drawn baseline from the absorption data in Fityk freeware. After that, the absorption peaks were fitted with Gaussian functions. The area of each absorption peak could then be calculated by integration of the Gaussian functions.

From the absorption area of the GeH bond at 560 cm^{-1}, the hydrogen content (N_H) was determined with the following relation [35]:

$$N_H = A \int \left(\frac{\alpha(\omega)}{\omega} \right) d\omega \approx A \cdot \frac{\ln(10) \cdot A_{abs}}{\omega_O \cdot d} \tag{4.2}$$

Where A is a proportionality constant, which is a function of dipole mass, frequency and effective charge [36], for which a value of 1.30×10^{19} cm^{-2} is taken [37]. Moreover, α(ω) is the absorption coefficient (cm^{-1}) at wavenumber ω (cm^{-1}), and d is the sample thickness

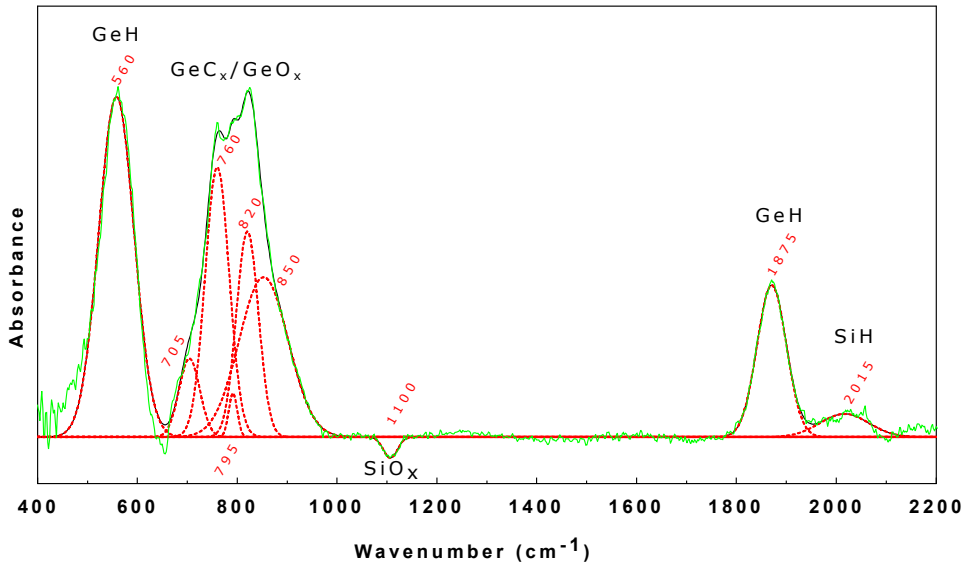

Figure 4.1: FTIR Absorbance spectrum of a Ge:H film with oxidation and carbon peaks

(cm). Furthermore, A_{abs} is the absorption area of the Gaussian at 560 cm^{-1} and ω_0 is the wavenumber at the center of the absorption peak. From N_H, the hydrogen concentration (C_H) was calculated as follows:

$$C_H = \frac{N_H}{N_{Ge}} \cdot 100 \tag{4.3}$$

Where C_H is the hydrogen concentration (%), N_H is the hydrogen content (cm^{-3}) and N_{Ge} is the atomic density of germanium (cm^{-3}), for which a value of 4.22×10^{22} cm^{-3} is used [38].

To quantitatively express the presence of various germanium-oxygen bonds (GeO_X), a thickness independent absorption coefficient, α_{GeO_X}, from de Vrijer et al. was used [36]. This metric is an indicator for multiple peaks in the range of 800-1050 cm^{-1} with peak centers roughly at 831, 846, 860, 930, 975 and 1000 cm^{-1}. α_{GeO_X} is calculated as follows:

$$\alpha_{GeO_X} = d^{-1} \cdot ln(10) \cdot \sum (A_{abs\ GeO_X}(\omega) \cdot \omega^{-1}) \tag{4.4}$$

Where d is the sample thickness (cm), $A_{abs\ GeO_X}(\omega)$ is the Gaussian area of the concerned GeO_X bond (cm^{-1}), and ω is the corresponding wavenumber (cm^{-1}). The "x" in α_{GeO_X} indicates that oxygen atoms can be bound to a germanium atom in various configurations.

For germanium-carbon bonds, a similar absorption coefficient (α_{GeC_X}) was used. This was done for FTIR absorbance peaks at 690 cm^{-1} [32], 767 cm^{-1} [33] and 773 cm^{-1} [33]. The following relation was used to calculate α_{GeC_X}:

$$\alpha_{GeC_X} = d^{-1} \cdot ln(10) \cdot \sum (A_{abs\ GeC_X}(\omega) \cdot \omega^{-1}) \tag{4.5}$$

For the samples that were processed and characterized in this thesis, complex peak-structures in the range of 700-1050 cm^{-1} were often observed. These signatures consist of many Gaussians, similar to the structure observed in figure 4.1. Because assigning absorption Gaussians of around 800 cm^{-1} to the presence of either GeC_x or GeO_x can be rather arbitrary, an absorption coefficient (α_{tot}) was used for the signature range of 700-1050 cm^{-1}. This coefficient was calculated by:

$$\alpha_{tot} = \alpha_{GeO_X} + \alpha_{GeC_X} \tag{4.6}$$

4.2. Spectroscopic ellipsometry

Spectroscopic ellipsometry (SE) is a characterisation method that measures a change in polarization of a light beam after interaction with a sample. From SE measurements, a variety of material properties can be derived. Figure 4.2 shows how polarized light is first emitted from a light source, then reflected by the sample, and finally measured with an optical detector. The interaction with the material causes the light beam to change from being linearly polarized to elliptically polarized. This change in polarization is dependent on sample thickness and its optical properties. Furthermore, the polarization change is quantified as a combination of amplitude ratio, ψ, and the phase difference Δ [11].

For this thesis, a J.A. Woollam M-2000 Ellipsometer was used to perform measurements on the glass substrate samples at a range of reflection angles from 55°-70°with respect to the normal. This range of angles lies around the Brewster angle of 62.5°. At the Brewster angle, the difference between the S- and P-polarized light is the largest. The measured wavelength range is from 190nm to 1700nm. After obtaining the measurement data, a Cody-Lorentz model was used to fit the data in the CompleteEASE software. When an optimal fit with an acceptable mean square error (MSE<10) was established, the following material properties were derived: refractive index for a wavelength of 600nm ($n_{@600nm}$), optical bandgap (E_{04}), Tauc bandgap energy (E_{Tauc}) and layer thickness.

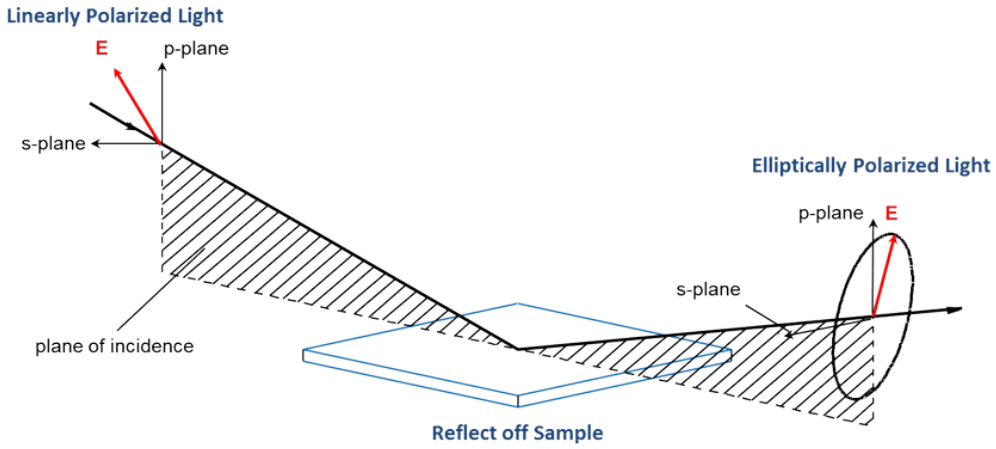

Figure 4.2: Spectral ellipsometry measurement setup using polarized light [11]

The E_{04} optical bandgap energy was derived from the wavelength at which the absorption coefficient equals $10^4\,cm^{-1}$ according to the fitted Cody-Lorentz model. In figure 4.3, the absorption coefficient of a typical Ge:H sample can be seen as function of wavelength for a range of roughly 200-1700 nm. In this work, E_{04} is chosen as main indicator for the bandgap of the material. It can be seen that the shown part of the absorption curve is quite dull and does not show a sharp drop or ”knee” that direct bandgap materials have. Because of this, the bandgap is less well defined. However, it can be seen in the graph that the E_{04} optical bandgap is at the steepest part of the curve, indicating a transitional point between two regions of the curve. Furthermore, the Tauc bandgap energy E_{Tauc} was derived directly from the fitted SE model.

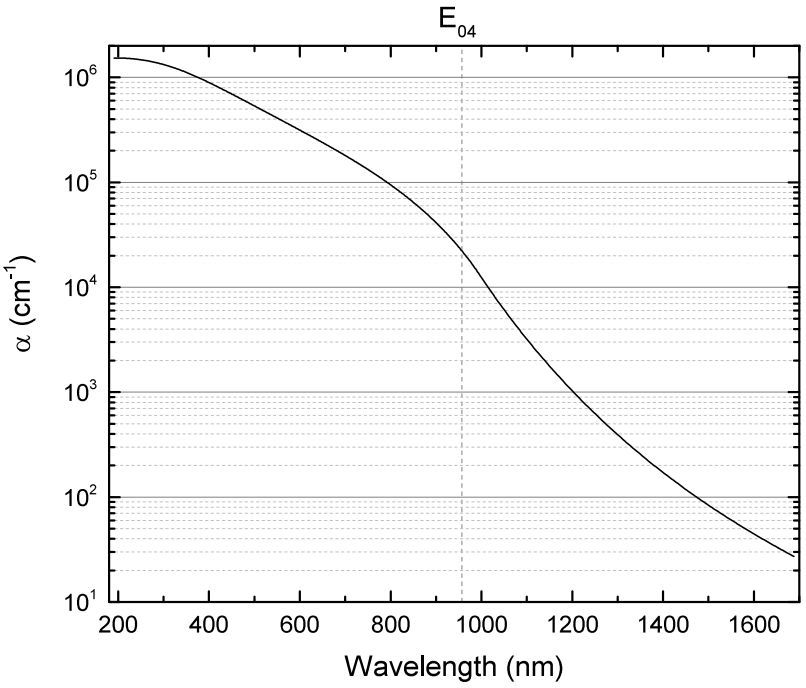

Figure 4.3: Absorption coefficient (α) as function of wavelength for a typical Ge:H film. The optical bandgap E_{04} corresponds to the absorption coefficient at $10^4\,cm^{-1}$.

4.3. Raman spectroscopy

Raman spectroscopy is a method used to identify vibrational modes of molecules in a material and relies on measuring the inelastic scattering of photons, known as Raman scattering. In this inelastic scattering process, the kinetic energy of an incident particle is not conserved, but transferred to the vibrational energy of a molecule. Vibrational energy can be lost or gained, causing a shift to higher or lower energy of the photons respectively.

The Raman spectroscopy measurements in this thesis were performed with a Renishaw inVia Raman microscope with an Argon 514nm green laser. This characterization method is used to determine the crystallinity of the Ge:H films by identification of amorphous and (nano)crystalline germanium bonds. Amorphous germanium has multiple Raman shift frequencies in the range of 80-280 cm^{-1} [39–41], whereas crystalline and nanocrystalline germanium has shift frequencies around 300 cm^{-1} [42–45]. The measured data was processed by fitting Gaussians at the following frequencies: 177 cm^{-1}, 230 cm^{-1}, 278 cm^{-1} and 300 cm^{-1}. The first three frequencies are respectively the longitudinal acoustic (LA), longitudinal optical (LO) and transversal optical (TO) stretching modes of amorphous germanium. The last frequency is the crystalline germanium peak. The Gaussian of the a-Ge transversal acoustic mode at 80 cm^{-1} was positioned outside the measurement range. The crystallinity was determined as ratio between the crystalline germanium peak and the largest amorphous stretching mode (TO mode) with a peak at 278 cm^{-1}:

$$X_C = \frac{I_{c-Ge}}{I_{c-Ge} + \gamma \cdot I_{a-Ge}} \tag{4.7}$$

Where X_C is the crystalline fraction, I_{c-Ge} is the area of the Gaussian fit related to crystalline germanium, γ is a correction factor that compensates for a difference in phonon excitation cross section between crystalline germanium and amorphous germanium, and I_{a-Ge} is the area of the Gaussian fit related to the amorphous germanium TO stretching mode.

4.4. Energy dispersive x-ray spectroscopy

Energy-dispersive X-ray spectroscopy (EDX) is an analytical technique used for elemental analysis of a sample. The method is based on x-ray excitation of atoms in a sample. After interaction with the sample, a detector measures the energy of the x-rays. Subsequently the measured data is processed and an energy spectrum can be obtained, which shows characteristic peaks for the elements that are present in the sample. For this thesis, EDX measurements were carried out with the FEI Nova NanoSEM 450 in the Kavli laboratory at TU Delft. These measurements were used to identify contaminants in the sample. Figure 4.4 shows the EDX spectrum of a typical Ge:H film. It can be observed that apart from germanium, also carbon and oxygen peaks are present. The oxygen peak indicates post-deposition oxidation and the appearance of an elemental carbon peak substantiates the assignment of GeC_x bonds to the FTIR peak position at around 760 cm^{-1}.

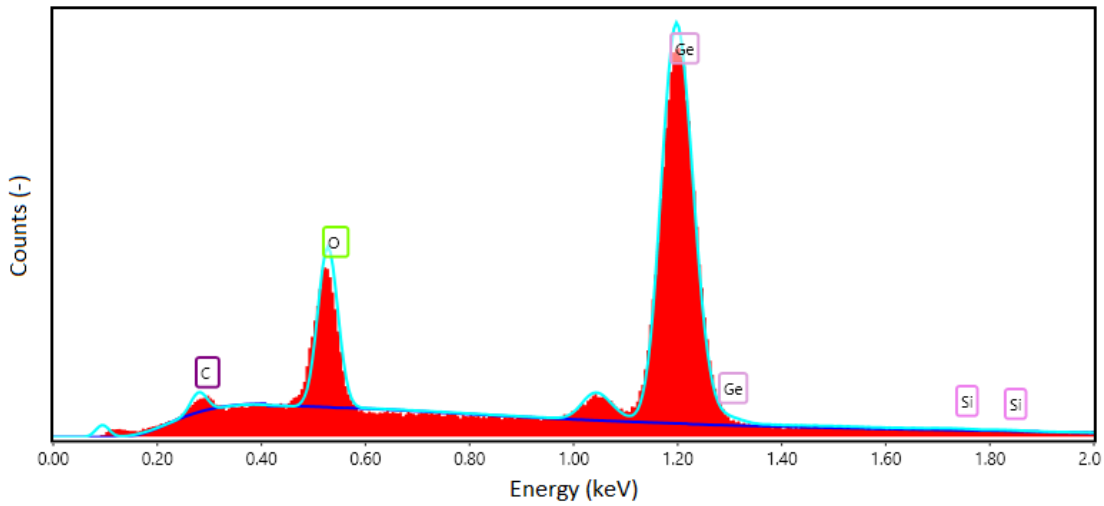

Figure 4.4: EDX spectrum of a typical Ge:H film

4.5. Photo conductivity measurement

Photovoltaic materials typically show an increase in electrical conductivity when illuminated. The conductivity of the material under these illuminated conditions is the photoconductivity σ_{ph}. In this research, photoconductivity measurements were performed with a WACOM AM1.5G solar simulator at an illumination of 100 mW cm^{-2} while maintaining a temperature of 25 °C. A voltage of 10V was applied between the contacts of the sample during the measurements. The photoconductivity could then be calculated as follows:

$$\sigma_{ph} = \frac{I}{V \cdot b \cdot d} \tag{4.8}$$

Where σ_{ph} is the photo conductivity (S cm^{-1}), I is the measured current (A), V the voltage (V), d the layer thickness (cm) and b a parameter that specifies the ratio of the contact length (the long side of the rectangular contact) over the gap between two contacts (-).

4.6. Dark conductivity measurement

The dark conductivity gives the material conductivity when no illumination is present and is an indicator for defects in a material. The measurements are performed in the dark by measuring the current between two contacts with an applied voltage of 10V. The used setup is a Micromanipulator Semi-Automatic Probe Station. The relation between dark conductivity and activation energy is given by the Arrhenius equation:

$$\sigma_d(T) = \sigma_0 \cdot e^{\frac{-Eact}{k_B T}} \tag{4.9}$$

Here σ_0 is a material dependent conductivity constant, k_B is the Boltzmann's constant and T is the temperature in Kelvin. It can be seen that the relation between the activation energy (E_{act}) and dark conductivity (σ_d) has an exponential temperature dependency. Hence, E_{act} can be determined in an experimental way with a Keithley 6517B electrometer by varying the temperature from 60-130 °C with steps of 5 °C and measuring the current through the sample at every temperature step. The dark conductivity was obtained from the dark current for each temperature step by using the following relation:

$$\sigma_d = \frac{I}{V} \cdot \frac{1}{b \cdot d} \tag{4.10}$$

Here σ_d is the dark conductivity (S cm^{-1}), I is the current (A), V is the voltage (V), b is a parameter that indicates the ratio of the contact length over the gap between the contacts and d is the sample thickness (cm). For this thesis, contacts with a b ratio of 40 were used by default.

The activation energy (E_{act}) was obtained from the dark conductivity measurements and indicates where the Fermi level is positioned between the conduction band and the valence band. The Fermi level represents the average energy level of an electron in a material. If the activation energy is low, less energy is required to excite an electron to the conduction band than at higher activation energies.

5

Results

For this thesis, 89 Ge:H films were PECVD processed with the objective of creating a device quality material that is stable, intrinsic and has a high photoresponse. To this end, the following three approaches were applied: I. Boron doping to increase the activation energy (E_{act}); II. Hydrogen plasma treatment (HPT) to decrease the defect density by the hydrogen passivation; III. A decreased electrode gap to improve the photoresponse. The results of these approaches will be discussed in the next three sections. A discussion on the observations related to post-deposition carbonation will follow in a subsequent section. Furthermore, a substantial fraction of the reported films was processed at an increased temperature of 275 °C. Comparison of film characteristics from these samples with the samples processed at 200 °C has revealed a strong influence of processing temperature (T_S) on the stability and opto-electrical properties of the hydrogenated germanium films. This influence will be considered in the final section of this chapter.

5.1. The influence of boron doping

It has been reported in earlier work that glow-discharge a-Ge:H films and PECVD Ge:H films have Fermi-levels close to the conduction band, making it n-type material with relatively low activation energies [8, 16–18]. In this work, an attempt has been made to increase the activation energy of the Ge:H films by adding boron to the plasma during the Ge:H film growth. Substrates with boron films were added to the substrate holder to function as boron donor. In figure 5.1, the results of this experiment can be seen. The blue bars correspond to amorphous samples with processing conditions of 2.5 W, 4 mbar, 100 $F(H_2)/F(GeH_4)$ and 275 °C. The green bars correspond to nanocrystalline samples with processing conditions of 5 mbar, 10 W, 400 $F(H_2)/F(GeH_4)$ and 275 °C. These two processing conditions were chosen because they correspond to an amorphous and a nanocrystalline phase. In this case, the amorphous samples have a crystallinity of lower than 2 % and the nanocrystalline samples have a crystallinity of 25 % or below. For both conditions, 2 reference samples were processed without boron doping, indicated by ”w/o”. The ”B1” samples were processed with boron doped films adjacent to the sample substrates for adding boron to the plasma. The ”B2” samples were processed similar to the ”B1” samples, but this time the boron films were exposed to a pure hydrogen plasma for 5min to assimilate boron in the plasma before starting the Ge:H deposition.

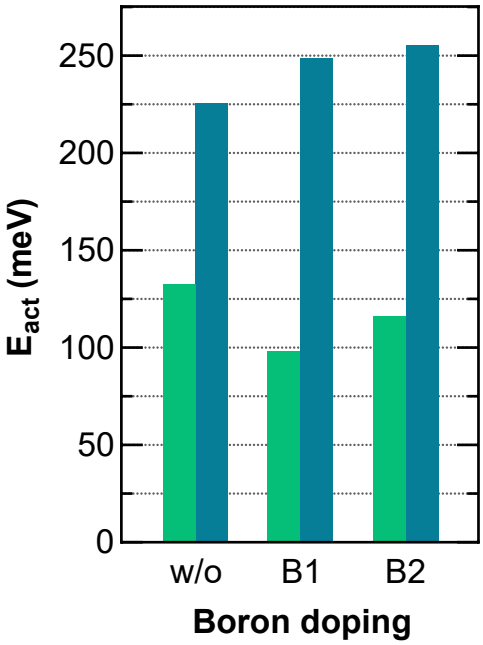

Figure 5.1: Influence of boron doping on the activation energy (E_{act}). On the x-axis the type of doping: without boron doping (w/o), with boron donor (B1) and with boron donor that has been exposed to a hydrogen plasma for 5 minutes before processing (B2). The blue bars correspond to amorphous conditions of 2.5W, 4mbar, 100 $F(H_2)/F(GeH_4)$ and 275 °C conditions. The green bars correspond to nano-crystalline conditions of 5mbar, 10W, 400 $F(H_2)/F(GeH_4)$ and 275 °C conditions.

It can be seen in the figure that the set of green bars have quite different E_{act} values (98-132 meV) from the set of blue bars (225-255 meV), indicating that the E_{act} is noticeable influenced by the processing conditions. However, when comparing the results of the boron doping procedures ”B1” and ”B2” with the ”w/o” reference samples it seems that the used boron doping procedures do not have a conclusive influence on E_{act}, as the E_{act} of the blue bars increase for ”B1” and ”B2”, and the E_{act} of the green bars show a decrease for ”B1” and ”B2”. Furthermore, the differences between the reference and boron doped samples for each condition are roughly 30 meV or less and seem to lie within the E_{act} error margin of 89 meV, which was obtained by considering the difference in E_{act} of two samples processed at exactly the same processing conditions. Therefore, the carried out boron doping experiment does not lead to a significant change in E_{act}.

5.2. The influence of hydrogen plasma treatment

In this section, the results of the hydrogen plasma treatment (HPT) experiments will be discussed. It was investigated if HPT could decrease the defect density of Ge:H films by hydrogen passivation. For this, processing conditions of 5 mbar 10 W 300 $F(H_2)/F(GeH_4)$ 11.5 mm electrode spacing and a T_S of 200 °C and 275 °C were chosen. Untreated reference samples for these conditions correspond to a relatively high σ_d of 7.5 $(m\Omega \cdot cm)^{-1}$ for the 200 °C condition and a low σ_d of 0.79 $(m\Omega \cdot cm)^{-1}$ for the 275 °C condition. The processing conditions of these two reference samples were reproduced for the HPT samples, to determine the influence of HPT on the defect density. Here, σ_d is considered as an indicator for the defect density, where a high σ_d corresponds to a high defect density. HPT was carried out directly after the Ge:H film deposition at varying powers of 1-20 W and with a pressure of 2.5 mbar for all HPT samples. The duration of the treatment was varied between 2-5-10 min and the HPT temperature was equal to T_S.

In figure 5.2 the influence of varying HPT powers on various material characteristics can be seen. Interesting is that the 200 °C samples (blue icons) show distinct differences with the 275 °C samples (red icons) for the shown graphs in this figure. The samples with elevated processing temperatures clearly have lower deposition rates, higher $n_{@600nm}$ values, lower GeO_x and GeC_x signature, and lower σ_d values. Furthermore it is remarkable that the samples processed at 275 °C have lower σ_d values than the 200 °C samples, while for σ_{ph}/σ_d no clear temperature dependence can be observed. Later in this chapter, we will discuss the influence of temperature on the Ge:H film characteristics in more detail and consider why an increased temperature of 275 °C does not lead to an increase of σ_{ph}/σ_d.

When evaluating the influence of HPT power and duration as shown in figure 5.2, it can be observed that the 275 °C samples that were HPT processed for 10 minutes have the highest $n_{@600nm}$ for most powers in combination with the lowest σ_d and a low GeO_x and GeC_x signature. Furthermore, the 10min 200 °C samples show also relatively high $n_{@600nm}$ in combination with relatively high E_{act} and low σ_d when compared to the 2min and 5min HPT treated samples of the same temperature. Furthermore, the 275 °C samples with a HPT duration of 10mins have a relatively low E_{04} for most powers. The samples with a HPT duration of only 2min have quite low E_{act} -relative to the longer HPT treated samples at the same temperature- for both the 200 °C samples and the 275°C samples. Furthermore, the samples with a HPT duration of 5min also have a quite high σ_d of above 7 $(m\Omega \cdot cm)^{-1}$ when compared to the 10min HPT treated samples of the same temperature. Overall, it seems that for both temperatures a longer HPT duration of 10min leads to lower porosity, indicated by $n_{@600nm}$, and lower defect density, indicated by σ_d when compared to the HPT treated samples of 2min and 5min. However, when compared to the reference samples that were not HPT treated (HPT power of 0W in graph), the 10min samples do not show a significant change for the shown material characteristics. Therefore it is not conclusive if the applied HPT conditions result in a significant change of material properties. Nonetheless, these results demonstrate a clear influence of processing temperature on the Ge:H film characteristics.

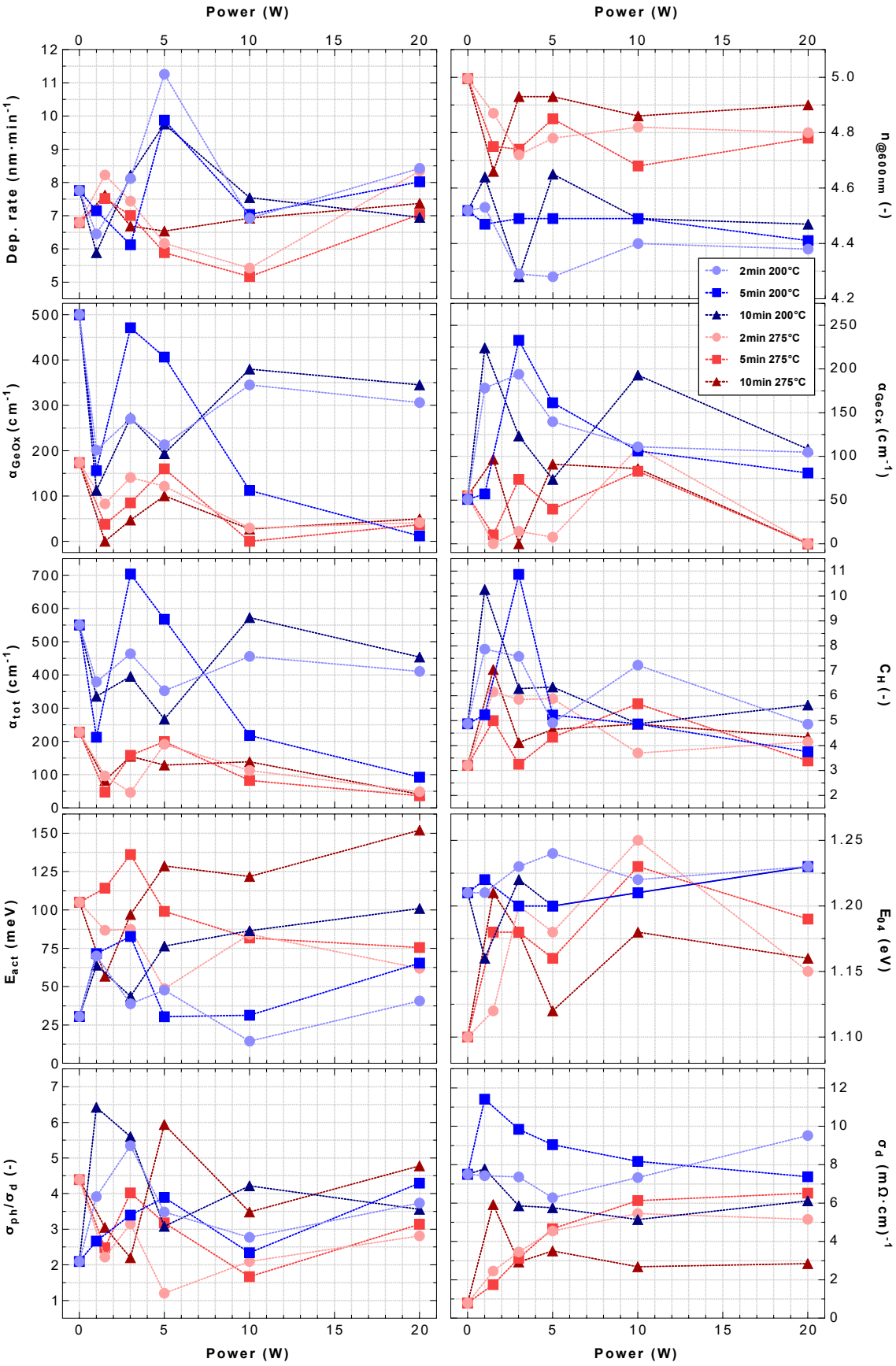

Figure 5.2: Hydrogen plasma treatment (HPT) of samples with Ge:H deposition conditions of 10W, 5mbar and temperatures of 200 °C and 275 °C as indicated by the blue and red icons respectively. The samples were hydrogen plasma treated for a duration of 2min, 5min or 10min. The HPT was carried out at the same temperature as the sample was processed and at a pressure of 2.5mbar for all samples. The samples with a power of 0W are reference samples without HPT.

5.3. Influence of a smaller electrode gap

The third approach was applied to investigate if higher σ_{ph}/σ_d could be obtained by decreasing the electrode gap from 20 mm to 11.5 mm. The influence of the electrode spacing on σ_{ph}/σ_d for PECVD Ge:H films was reported by W. Paul, who discovered that a higher photo-response was achieved for films that were processed at smaller electrode gaps [19]. An electrode gap of 11.5 mm was applied, as for smaller electrode gaps than 11.5 mm no stable plasma could be established. Exploration of the processing window for a 20 mm electrode gap was carried out in earlier research by B. Bouazzata and A. Ravichandran under supervision of T. de Vrijer and A. Smets. In their work σ_{ph}/σ_d values in the range of 1-6 were reported. These Ge:H films were processed in the same reactor with a similar procedure as the samples for this thesis. Because the Ge:H film deposition mechanisms are influenced by the distance between the electrodes, a processing window was explored to find the optimal processing conditions for the 11.5 mm spacing. For this, the following conditions were used: 2.5-5-10W, 1-2-3-4-5/6 mbar, $F(H_2)/F(GeH_4)$ of 100-200-300-400 and 200-275 °C. The processing window was explored only for relatively low powers of 2.5-10W (compared to 5-30 W at 20 mm), because at smaller electrode spacing lower powers could be used (to sustain the plasma), thereby enabling lower deposition rates for denser material growth. The correlation between lower powers and denser films was observed by [8, 16, 17], who reported that relatively dense films with a low oxidation signature were obtained for powers of 5W. Figure 5.3, shows the powers and pressures of the processing window together with the crystallinity X_C depicted by the colored symbols. It can be observed that at lower powers of 2.5 W and 5 W, X_C is 0 for all pressures. Furthermore, it can be observed that at 10W, a combination of crystalline and amorphous phases is present. In the next subsection, the influence of power and pressure on the film characteristics will be discussed for the 11 5mm spacing and subsequently the influence of $F(H_2)/F(GeH_4)$ will be discussed.

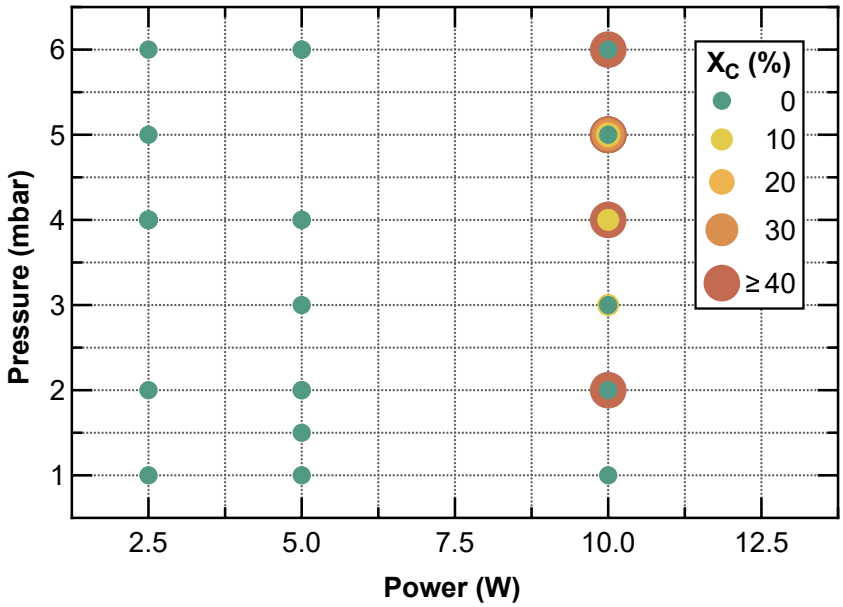

Figure 5.3: Pressure and power of all processed Ge:H films with the level of crystallinity indicated by the color and size of the icons.

5.3.1. Influence of pressure and power

In this section the influence of varying power and pressure will be discussed. Figure 5.4 displays an overview with characterization results from this sample set. The samples from this set are processed with $F(H_2)/F(GeH_4)$ of 200 and 400. The processing powers are varied at 2.5W, 5W and 10W. The pressure is varied at 1 mbar, 2 mbar, 3 mbar, 4 mbar, 5 mbar and 6 mbar. Furthermore, the processing temperature is kept constant at 200 °C. For lower pressure and power conditions, a stable plasma could not always be generated, therefore no sam-

ples were made at these conditions. For the 400 $F(H_2)/F(GeH_4)$ 5W sample, 1.5W was taken as processing power instead of 1W for the same reason. The 3 mbar 5 W 400 $F(H_2)/F(GeH_4)$ sample was omitted because of a large deviation in layer thickness with respect to the rest of the samples.

Now the results of this sample set will be discussed with the help of the plots in figure 5.4 and underlying mechanisms will be considered. The deposition rate increases quite linearly with increasing pressure, which could be explained by the availability of more precursor molecules, causing an increased Ge growth flux. This increased Ge growth flux leads to higher void incorporation in the material, increasing the porosity, which can be seen by the increased $n_{@600nm}$. This trend can be linked to the increased α_{tot} for higher pressures, indicating increased oxidation and carbonation for more porous films. E_{act} shows a decrease for samples with higher α_{tot}, which can be attributed to the introduction of defect states close to the conduction band. The E_{act} increase for low powers of 2.5 W might be caused by the filling of small voids at higher pressures, resulting in a decreased defect density, as demonstrated by the low σ_d. For E_{04}, the 5W samples show a decrease as the pressure increases, where the other samples show more deviation or an upward trend. The 400 H_2 dilution sample at 4mbar does not have an E_{04} value, because the absorption coefficient for this sample was above $1 \times 10^4\,cm^{-1}$ for the measured SE wavelength range. The dark conductivity graph shows an exponential relation between σ_d and pressure for most samples, as can be seen by the straight lines in combination with the logarithmic σ_d axis. The decrease in σ_d for increasing pressures can be contributed to increased passivation by post-deposition oxidation.

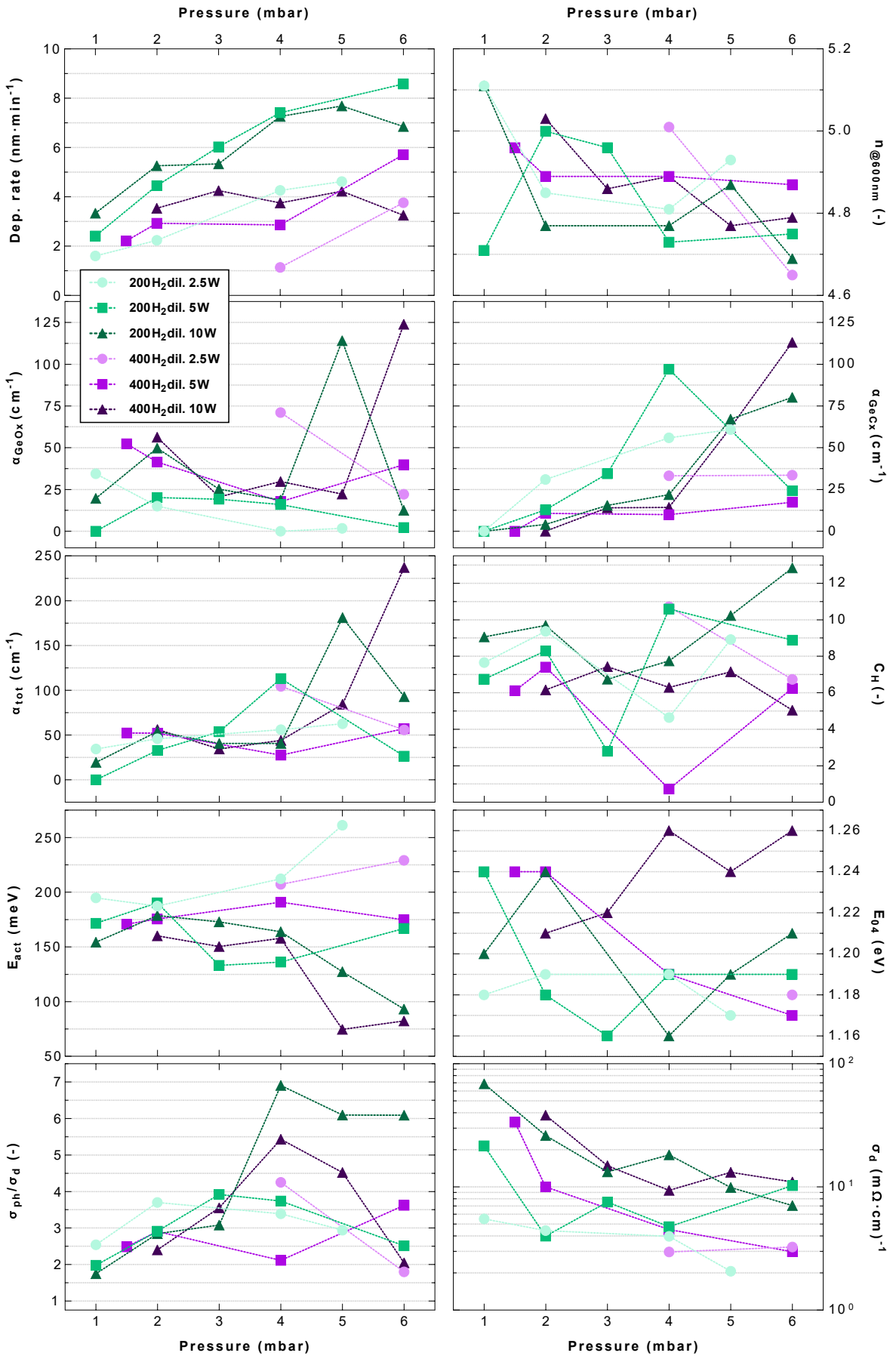

Figure 5.4: Influence of pressure on the Ge:H film characteristics. The colored icons indicate $F(H_2)/F(GeH_4)$ and power (W). An outlier of the $n_{@600nm}$ graph with conditions of 3 mbar 10 W 200 $F(H_2)/F(GeH_4)$ was omitted.

5.3.2. Influence of GeH_4 in H_2 dilution

In this subsection, the influence of varying $F(H_2)/F(GeH_4)$ on the material characteristics will be discussed. Two sets of conditions were chosen: one with high E_{act} that was amorphous for 100 and 400 $F(H_2)/F(GeH_4)$ and one with low E_{act} that was amorphous for 100 $F(H_2)/F(GeH_4)$ and nano-crystalline for 400 $F(H_2)/F(GeH_4)$. The first set of conditions had pressure and power of 4 mbar 2.5 W and the second had pressure and power of 5 mbar 10 W. Both sets of conditions were processed for 100-200-300-400 $F(H_2)/F(GeH_4)$ and at a T_S of 200 °C and 275 °C. Figure 5.5 shows the results for these sets of conditions. The plot with the deposition rate clearly shows that the samples with the same pressure and power have quite similar deposition rates. The deposition rate drops for increasing dilution ratio, which could be a result of increased atomic hydrogen etching or it could be a consequence of a lower availability of germanium radicals to grow the material [36]. Furthermore, the combination of higher power and pressure results in much higher deposition rates, caused by the increased Ge-radical flux towards the film surface. Furthermore, it can be observed that a combination of lower pressure and power leads to higher $n_{@600nm}$ and moreover, higher temperatures also lead to higher $n_{@600nm}$. The plot with the hydrogen content (C_H) shows that for most samples, C_H slightly decreases for increasing $F(H_2)/F(GeH_4)$. The α_{GeO_x} plot shows that the 4 mbar samples have very low α_{GeO_x} values of below 50 cm^{-1}. When looking at the α_{GeC_x} values, the samples processed at 4 mbar 2.5 W and 275 °C have none or low carbon contamination. This corresponds to a relatively high E_{act} of up to 314 meV. This is likely the consequence of decreased post-deposition and carbonation at higher temperatures, as less defect states are introduced close to the conduction band. E_{04} shows higher values for the samples processed at 200 °C, which could also be explained by increased sub-bandgap absorption as a result of increased post-deposition oxidation. σ_{ph}/σ_d shows a general upward trend over increased $F(H_2)/F(GeH_4)$. This corresponds to a decrease in σ_d for samples with larger oxygen and carbon contamination, as can be seen in the plot of σ_d. Therefore, it seems likely that this decrease in dark conductivity can be attributed to the defect passivation in a/nc-Ge:H films by oxygen as suggested in the work of [36].

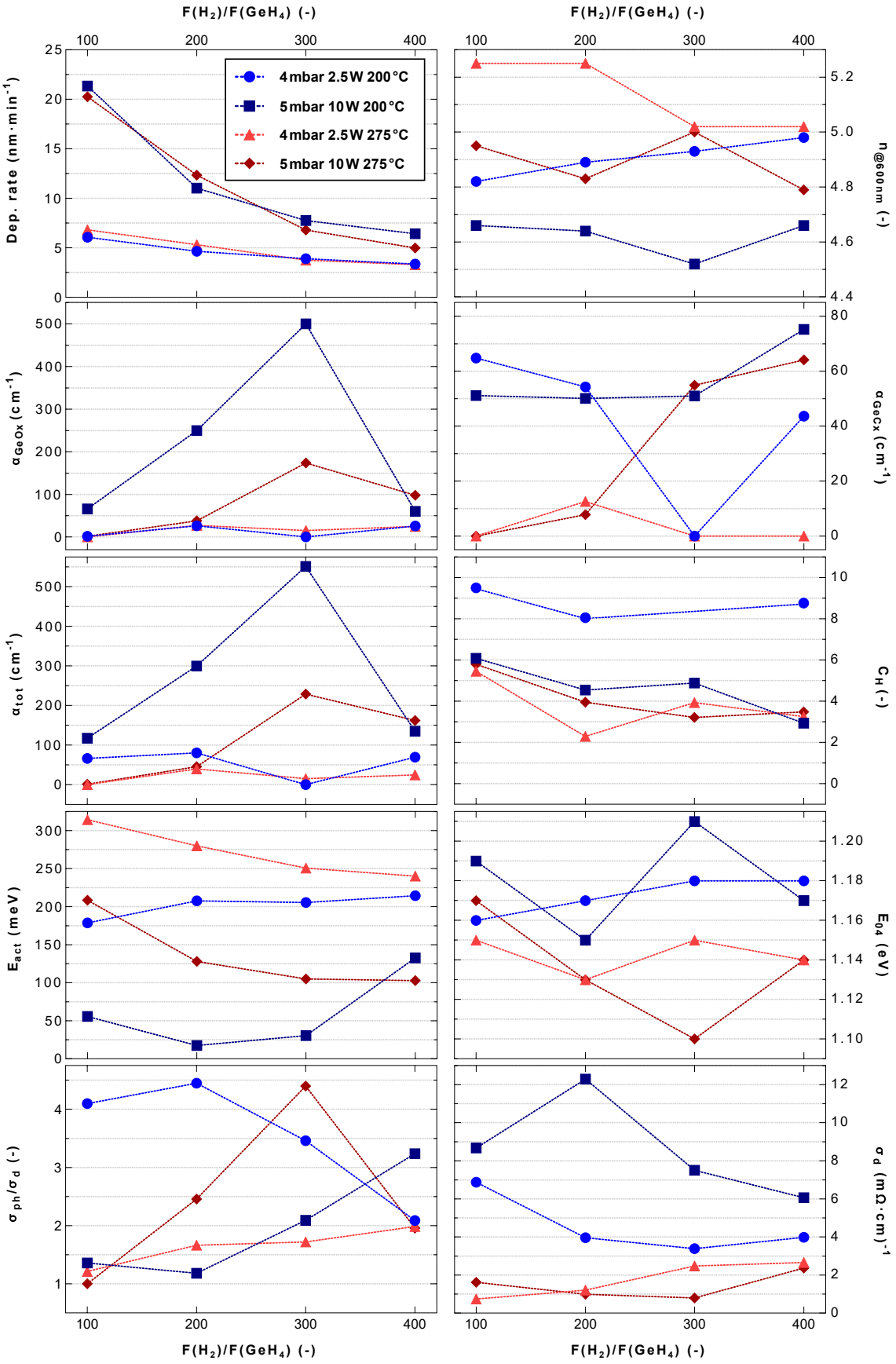

Figure 5.5: Influence of $F(H_2)/F(GeH_4)$ on the Ge:H film characteristics. The variation in pressure, power and temperature are depicted by the colored symbols.

5.4. Post-deposition carbonation

This section discusses the origin of carbon in the Ge:H films. With EDX measurements, the presence of carbon in the material was demonstrated and with FTIR peaks at around 760 cm^{-1} were observed that are associated with GeC_x bonds. Degradation experiments were carried out for various germanium alloys by T. de Vrijer and B. Bouazzata to investigate the stability of these alloys. Figure 5.6 shows the FTIR absorbance of nc-Ge:H and a-GeC:H films exposed to light, water and air (in the dark) for varying duration. Indicated is the peak position at roughly 760 cm^{-1}, which is associated with GeC_x. For the a-GeC:H absorption spectrum, it can be observed that after conditions of water 10hrs, dark 100hrs and light 10hrs, an widening peak-structure at around 760 cm^{-1} is present, which is increasing in reference to the 560 cm^{-1} GeH peak, indicating progressive post-deposition formation of GeO_x and GeC_x bonds. In the absorption spectrum of the nc-Ge:H films, a growing signature in the 2800-3000 cm^{-1} range can be observed. These peak positions are associated with CH_x bonds [46]. Therefore, growth of this signature over time indicates a post-deposition carbonation reaction, most likely with an ambient CO_2 origin as this seems to be the only carbon source that is present during the degradation of the samples. Consequently, the signature growth over time for these two peak positions seems to suggest the occurrence of a catalytic CO_2 reduction reaction.

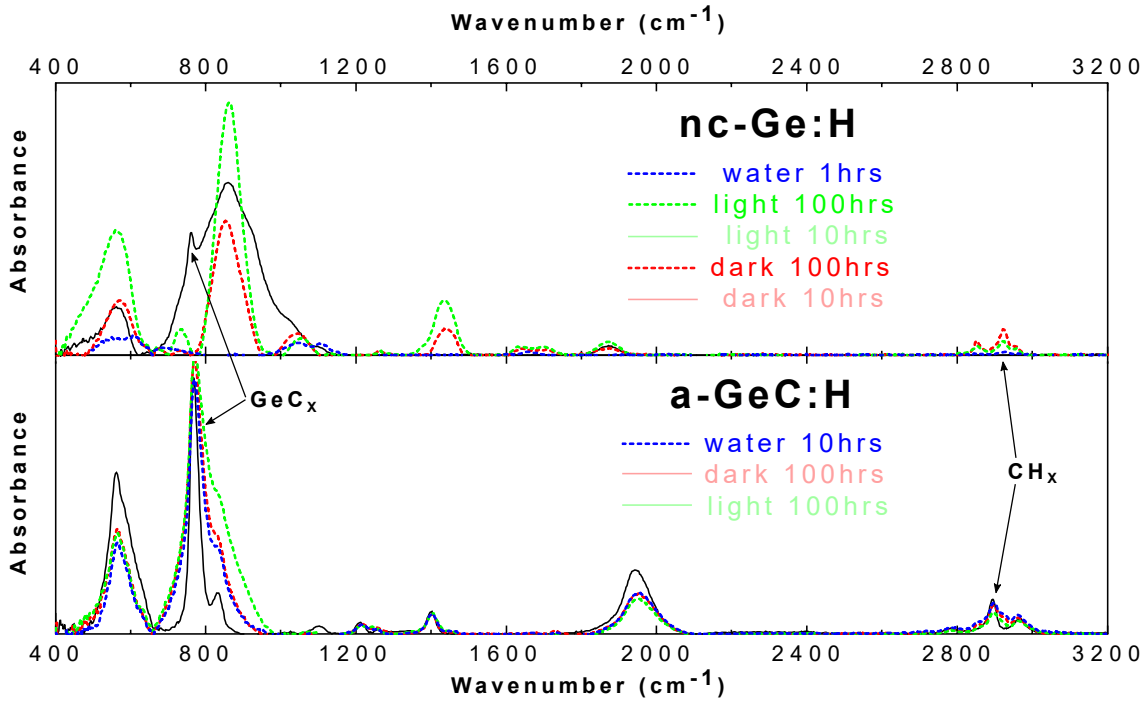

Figure 5.6: FTIR of nc-Ge:H and a-GeC:H films exposed to light, water and air for varying duration. Indicated is the GeC_x peak position at roughly 760 cm^{-1} and peak positions at 2800-3000 cm^{-1} associated with HCHO. Figure from [47].

5.5. The influence of temperature

The results from 5.2 and 5.3.2 show that processing temperature (T_S) has a strong influence on the Ge:H film properties. In this section, this temperature effect will be investigated in more detail. In figure 5.7 σ_{ph}, σ_d and σ_{ph}/σ_d are shown with their relation to T_S, $n_{@600nm}$ and α_{tot}. This figure shows that higher $n_{@600nm}$ values, associated with denser films, were obtained for a T_S of 275 °C. It is suggested that a dense material prevents the in-diffusion of ambient CO_2 and/or H_2O into the Ge:H network. As a result, these denser films show very low α_{tot}.

When considering the correlation between T_S and $n_{@600nm}$, we speculate that at increased temperatures voids have higher mobility, enabling voids to move towards the surface and leave the material, thereby decreasing the void density and increasing the film density.

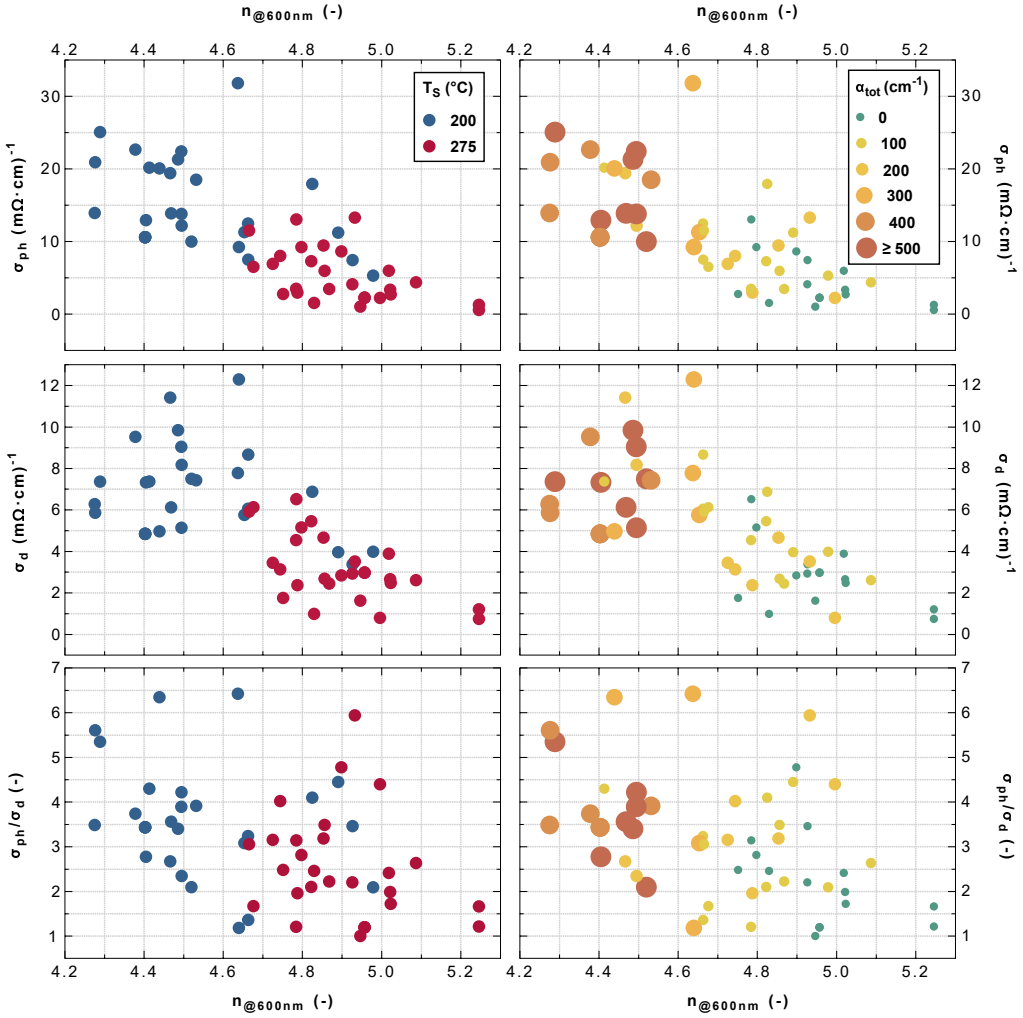

Figure 5.7: From top to bottom: influence of T_S (top), $n_{@600nm}$ (middle) and α_{tot} (bottom) on σ_{ph}, σ_d and σ_{ph}/σ_d. Note that a correction factor was applied to the σ_{ph}/σ_d values to adjust for a discrepancy between the measured σ_d and σ_{ph}.

Lastly, it will be considered why an increased T_S of 275 °C leads to lower σ_d but does not lead to increased σ_{ph}/σ_d. It seems that this is caused by a proportional decrease of both σ_d and σ_{ph}, resulting in a roughly equal σ_{ph}/σ_d range for both temperatures. A possible explanation for this could be that the defect density is still quite high, thereby inhibiting the improvement of the photoresponse. Therefore, to improve the photoresponse, a further reduction of the defect density is required.

6

Conclusion and recommendations

6.1. Conclusion

For this thesis, 89 amorphous/nano-crystalline hydrogenated germanium (a-/nc-Ge:H) films were PECVD processed with the objective of creating a device quality material that is stable, intrinsic and has a high photoresponse. These characteristics are required to enable p-i-n bottom cell integration in a multi-junction device and prevent post-deposition oxidation and carbonation. To this end, the following three approaches were applied: I. Boron doping to increase the activation energy. II. Hydrogen plasma treatment (HPT) to decrease the defect density of the material by hydrogen passivation. III. A decreased electrode gap to improve the photoresponse. These approaches were integrated in the sample preparation steps. Subsequent film characterization was carried out by using vibrational analysis, elemental analysis, and opto-electrical analysis. Below, the findings of each approach will be briefly explained. Furthermore, a short discussion on post-deposition carbonation will follow and finally the strong influence of temperature on the material properties will be considered.

I. Boron doping

Boron doping was carried out by placing boron films adjacent to the sample substrates for amorphous and nanocrystalline processing conditions. The boron doped amorphous samples showed a slight increase of E_{act} compared to the reference sample, where the boron doped nanocrystalline samples showed a slight decrease of E_{act} compared to the reference sample. These deviations can be considered as relatively small (ΔE_{act}<30 meV) relative to the error margin of 89 meV, which was obtained by taking the difference in E_{act} of two samples processed at exactly the same processing conditions. Therefore, the carried out boron doping experiment does not lead to a significant change in E_{act}.

II. Hydrogen plasma treatment

Hydrogen plasma treatment (HPT) was carried out by exposing the Ge:H films to a pure hydrogen plasma after PECVD. HPT was applied with a power of 1-10 W, a duration of 2-10 min and for processing temperatures (T_S) of 200 °C and 275 °C. The influence of HPT on the defect density and other material characteristics was not found to be conclusive. However, a significant influence of T_S on the material characteristics was observed. The samples processed at an increased temperature of 275 °C showed a higher $n_{@600nm}$, indicating a denser material; lower σ_d, indicating a lower defect density; and lower GeO_x and GeC_x signatures. Despite, lower σ_d, the photoresponse, indicated by the photo-/dark conductivity ratio (σ_{ph}/σ_d) did not increase. σ_{ph}/σ_d values in the range of 1-7 were observed.

III. Decreased electrode gap

The third approach was applied to investigate if higher σ_{ph}/σ_d could be obtained for a decreased electrode gap of 11.5 mm in comparison to a larger electrode gap of 20 mm. For smaller electrode gaps than 11.5 mm, no stable plasma could be established. Because the

Ge:H film deposition mechanism is influenced by the width of the electrode gap, a processing window was explored to find the optimal processing conditions for the decreased electrode gap. For this processing window, the following conditions were used: 2.5-10 W, 1-6 mbar, 100-400 $F(H_2)/F(GeH_4)$ and 200-275 °C. For this decreased electrode gap of 11.5 mm, it was found that lower deposition rates of 1-4 nm min^{-1} in combination with higher $n_{@600nm}$ of 4.9-5.0 could be achieved (for conditions of 400 $F(H_2)/F(GeH_4)$ 2.5-5 W 1-4 mbar and 200 °C), whereas the same conditions with a larger electrode gap of 20mm resulted in higher deposition rates of 1-6 nm m^{-1} with lower $n_{@600nm}$ of 4.1-4.9. Furthermore, a pressure related trend was observed.

An increase of pressure from 1-6 mbar corresponds to a general decrease of $n_{@600nm}$ (5.1-4.7 for instance for 200 $F(H_2)/F(GeH_4)$ 10 W 200 °C), indicating an increase in film porosity. This increased porosity corresponds with increased post-deposition oxidation and carbonation. The decrease of $n_{@600nm}$ can be attributed to the increased Ge-growth flux at increased pressure, leading to higher void incorporation in the material, resulting in a more porous film.

Post-deposition carbonation
With EDX measurements, the presence of carbon in the material was demonstrated and with FTIR peaks at around 760 cm^{-1} were observed that are associated with GeC_x bonds. The origin of these bonds was investigated by exposing nc-Ge:H and a-GeC:H to water, light and air (in the dark) for varying duration. At the FTIR peak position of 760 cm^{-1}, an over time growing signature was observed for a-GeC:H. Furthermore, at peak positions in the range of 2800-3000 cm^{-1}, a growing signature associated with CH_x was observed for nc-GeC:H. As no other carbon sources were present, the growth of these signatures seems to suggest the occurrence of a (catalytic) CO_2 reduction reaction from ambient CO_2.

Influence of temperature
A T_S increase from 200 °C to 275 °C corresponds to a significant increase of $n_{@600nm}$ (up to 5.2), increase of E_{act} (up to 314 meV) and decrease of GeO_x and GeC_x signature. We speculate that this effect is caused by increased void mobility at the increased temperature of 275 °C, thereby enabling voids to move to the film surface and leave the material, resulting in denser films. Furthermore, the increased film density of these samples seems to prevent the in-diffusion of molecules from the ambient into the Ge:H network that cause the formation of GeO_x and GeC_x bonds. Therefore, by increasing the processing temperature, it was accomplished to produce denser, more stable films, which have a lower bandgap energy and are more intrinsic.

6.2. Recommendations

This research has showed steps to increase the Ge:H film stability. To make a device quality low bandgap absorber layer, a significant increase in photoresponse (σ_{ph}/σ_d) is required in combination with a further increase of E_{act} and a decrease of bandgap (E_{Tauc} and E_{04}). The following four recommendations could be worthwhile to consider for further research.

Firstly, to figure out if boron doping has a conclusive influence on the E_{act}, a larger sample set needs to be processed, for which the boron doping is preferably applied by adding boron in the form of a precursor gas instead of the used method of exposing a boron doped film to the plasma during deposition.

Secondly, it would be interesting to alloy germanium with tin (Sn), similar to the alloying of silicon with germanium. With this GeSn material a lower bandgap could be obtained of 0.6-1.0 eV [48] and development of such an alloy could be a step towards achieving decreased defect densities, leading to a higher photoresponse.

Furthermore, it would be useful to further investigate the effect of T_S on $n_{@600nm}$. By investigating the effect of varying temperature in a range around 275 °C (e.g. 250-300 °C), it

can be observed how varying T_S influences $n_{@600nm}$, thereby acquiring more insight in the film growth process. Processing at above 300 °C might also be favorable for the film characteristics, but this could raise issues for some parts of the CASCADE system, as the limits of their operational temperature range are exceeded.

Lastly, the presence of GeC bonds in the material is quite intriguing. In case this carbon originates from atmospheric CO_2, as is speculated in this thesis, it would indicate that some form of catalytic CO_2 reduction occurs within the material. Obviously, this is still quite speculative and further research is required to substantiate these theories.

Bibliography

[1] V. Smil, *Energy transitions*, 2nd ed. Praeger, 2016.

[2] B. Dudley *et al.*, "Bp statistical review of world energy," *BP Statistical Review, London, UK, accessed Aug*, vol. 6, p. 2018, 2019.

[3] 2020. [Online]. Available: https://www.ise.fraunhofer.de/content/dam/ise/de/documents/publications/studies/Photovoltaics-Report.pdf

[4] D. Álvarez, "Solar energy, that great unknown - sruk," 2020. [Online]. Available: https://sruk.org.uk/solar-energy-that-great-unknown-2/

[5] T. de Vrijer and A. Smets, "a-/nc-gesn:h thesis description," Master thesis description, 2020.

[6] A. H. Smets, K. Jäger, O. Isabella, R. A. Swaaij, and M. Zeman, *Solar energy: The physics and engineering of photovoltaic conversion, technologies and systems*. UIT Cambridge, 2015.

[7] M. A. Rind, "Photovoltaic applications of si and ge thin films deposited by pecvd," Ph.D. dissertation, University of Southampton, 2014.

[8] T. de Vrijer, A. Ravichandran, B. Bouazzata, and A. H. Smets, "The impact of processing conditions and post-deposition oxidation on the opto-electrical properties of hydrogenated amorphous and nano-crystalline germanium films," *Journal of Non-Crystalline Solids*, vol. 553, p. 120507, 2021.

[9] P. Babál, "Doped nanocrystalline silicon oxide for use as (intermediate) reflecting layers in thin-film silicon solar cells," 2014.

[10] G. Papakonstantinou, "Investigation and optimization of the front metal contact of silicon heterojunction solar cells," Master's thesis, Delft University of Technology, 2014.

[11] J. W. E. Solutions, "What is ellipsometry?" [Online]. Available: https://www.jawoollam.com/resources/ellipsometry-tutorial/what-is-ellipsometry?

[12] P. Espinosa, "The paris agreement, a strategy for the longer term," 2020. [Online]. Available: https://www.wri.org/climate/expert-perspective/paris-agreement-strategy-longer-term

[13] B. S. Alharthi, "Growth and characterization of silicon-germanium-tin semiconductors for future nanophotonics devices," Ph.D. dissertation, University of Arkansas, Fayetteville, 2018.

[14] 2020, accessed 10-12-2020. [Online]. Available: https://www.irena.org/-/media/Files/IRENA/Agency/Publication/2020/Apr/IRENA_GRO_Summary_2020.pdf?la=en&hash=1F18E445B56228AF8C4893CAEF147ED0163A0E47

[15] 2020. [Online]. Available: http://www.world-nuclear.org/uploadedFiles/org/WNA/Publications/Working_Group_Reports/comparison_of_lifecycle.pdf

[16] B. Bouazzata, "Development of a-/nc-ge:h; growth and characterization of a low bandgap material," Master's thesis, Delft University of Technology, 2020.

[17] A. N. Ravichandran, "Development of a-/nc-ge:h; film characterization and single-junction solar cell," Master's thesis, Delft University of Technology, 2020.

[18] M. Stutzmann, J. Stuke, and H. Dersch, "Electron spin resonance of doped glow-discharge amorphous germanium," *physica status solidi (b)*, vol. 115, no. 1, pp. 141–151, 1983.

[19] W. Paul, "Structural, optical and photoelectronic properties of improved pecvd a-ge: H," *Journal of non-crystalline solids*, vol. 137, pp. 803–808, 1991.

[20] M. F. Modest, *Radiative Heat Transfer*. Academic press, 2013, ch. Fundamentals Of Thermal Radiation, p. 6.

[21] P. Faine, S. R. Kurtz, C. Riordan, and J. Olson, "The influence of spectral solar irradiance variations on the performance of selected single-junction and multijunction solar cells," *Solar cells*, vol. 31, no. 3, pp. 259–278, 1991.

[22] K. Yokoi, *Germanium, Toxicity*. New York, NY: Springer New York, 2013, pp. 842–846. [Online]. Available: https://doi.org/10.1007/978-1-4614-1533-6_434

[23] R. Höll, M. Kling, and E. Schroll, "Metallogenesis of germanium—a review," *Ore Geology Reviews*, vol. 30, no. 3-4, pp. 145–180, 2007.

[24] D. Stewart, "Germanium," 2020. [Online]. Available: http://www.chemicool.com/elements/germanium.html

[25] M. Moreno, R. Ambrosio, A. Torres, A. Torres, P. Rosales, A. Itzmoyotl, and M. Domínguez, "Amorphous, polymorphous, and microcrystalline silicon thin films deposited by plasma at low temperatures," *Crystalline and Non-crystalline Solids*, p. 147, 2016.

[26] V. L. Dalal, S. Kaushal, J. Xu, and K. Han, "A critical review of the growth and properties of a-(si, ge): H," in *Proceedings of 1994 IEEE 1st World Conference on Photovoltaic Energy Conversion-WCPEC (A Joint Conference of PVSC, PVSEC and PSEC)*, vol. 1. IEEE, 1994, pp. 464–467.

[27] W. van Sark, L. Korte, and F. Roca, *Physics and technology of amorphous-crystalline heterostructure silicon solar cells*. Springer, 2012.

[28] W. Kusian, H. Pfleiderer, and E. Günzel, "Electron and hole $\mu\tau$ products of slightly doped a-ge: H films," *Journal of non-crystalline solids*, vol. 137, pp. 813–816, 1991.

[29] F. Karg, H. Böhm, and K. Pierz, "Influence of plasma deposition on structural and electronic properties of a-ge: H," *Journal of Non-Crystalline Solids*, vol. 114, pp. 477–479, 1989.

[30] A. Descoeudres, L. Barraud, S. De Wolf, B. Strahm, D. Lachenal, C. Guérin, Z. Holman, F. Zicarelli, B. Demaurex, J. Seif *et al.*, "Improved amorphous/crystalline silicon interface passivation by hydrogen plasma treatment," *Applied Physics Letters*, vol. 99, no. 12, p. 123506, 2011.

[31] K. Saitoh, M. Kondo, M. Fukawa, T. Nishimiya, A. Matsuda, W. Futako, and I. Shimizu, "Role of the hydrogen plasma treatment in layer-by-layer deposition of microcrystalline silicon," *Applied physics letters*, vol. 71, no. 23, pp. 3403–3405, 1997.

[32] H. Jamali, R. Mozafarinia, and A. Eshaghi, "Evaluation of chemical and structural properties of germanium-carbon coatings deposited by plasma enhanced chemical vapor deposition," *Journal of Alloys and Compounds*, vol. 646, pp. 360–367, 2015.

[33] J. Szmidt, M. Gazicki-Lipman, H. Szymanowski, R. Mazurczyk, A. Werbowy, and A. Kudła, "Electrophysical properties of thin germanium/carbon layers produced on silicon using organometallic radio frequency plasma enhanced chemical vapor deposition process," *Thin Solid Films*, vol. 441, no. 1-2, pp. 192–199, 2003.

[34] A. Smets, T. Matsui, and M. Kondo, "High-rate deposition of microcrystalline silicon p-i-n solar cells in the high pressure depletion regime," *Journal of Applied Physics*, vol. 104, no. 3, p. 034508, 2008.

[35] A. Kosarev, A. Torres, Y. Hernandez, R. Ambrosio, C. Zuniga, T. Felter, R. Asomoza, Y. Kudriavtsev, R. Silva-Gonzalez, E. Gomez-Barojas *et al.*, "Silicon-germanium films deposited by low frequency pe cvd: Effect of h2 and ar dilution," *Journal of the Materials Research Society*, vol. 21, no. UCRL-JRNL-215632, 2005.

[36] T. de Vrijer, A. N. Ravichandran, B. Bouazzata, and A. Smets, "Characterisation of amorphous and nanocrystalline germanium films," 2020, Delft University of Technology.

[37] M. Abo-Ghazala and S. A. Hazrny, "Hydrogen bonding in hydrogenated amorphous germanium," *Tsinghua Science and Technology*, vol. 9, no. 2, pp. 177–180, 2004.

[38] 2021. [Online]. Available: https://eesemi.com/sigegaas.htm

[39] D. Bermejo and M. Cardona, "Raman scattering in pure and hydrogenated amorphous germanium and silicon," *Journal of Non-Crystalline Solids*, vol. 32, no. 1-3, pp. 405–419, 1979.

[40] V. Volodin, G. Krivyakin, G. Ivlev, S. Prokopyev, S. Gusakova, and A. Popov, "Crystallization of amorphous germanium films and multilayer a-ge/a-si structures upon exposure to nanosecond laser radiation," *Semiconductors*, vol. 53, no. 3, pp. 400–405, 2019.

[41] M. Stutzmann, R. Street, C. Tsai, J. Boyce, and S. Ready, "Structural, optical, and spin properties of hydrogenated amorphous silicon-germanium alloys," *Journal of applied physics*, vol. 66, no. 2, pp. 569–592, 1989.

[42] Y. Maeda, "Visible photoluminescence from nanocrystallite ge embedded in a glassy sio 2 matrix: evidence in support of the quantum-confinement mechanism," *Physical Review B*, vol. 51, no. 3, p. 1658, 1995.

[43] V. Volodin, D. Marin, V. Sachkov, E. Gorokhov, H. Rinnert, and M. Vergnat, "Applying an improved phonon confinement model to the analysis of raman spectra of germanium nanocrystals," *Journal of Experimental and Theoretical Physics*, vol. 118, no. 1, pp. 65–71, 2014.

[44] P. Klement, C. Feser, B. Hanke, K. v. Maydell, and C. Agert, "Correlation between optical emission spectroscopy of hydrogen/germane plasma and the raman crystallinity factor of germanium layers," *Applied Physics Letters*, vol. 102, no. 15, p. 152109, 2013.

[45] P. Alfaro-Calderón, M. Cruz-Irisson, and C. Wang-Chen, "Theory of raman scattering by phonons in germanium nanostructures," *Nanoscale Research Letters*, vol. 3, no. 2, pp. 55–59, 2008.

[46] Y. Yamashita, N. Ikeno, N. Aizawa, T. Tachibana, Y. Ohshita, and A. Ogura, "Raman spectroscopy study of crystalline damage induced by pecvd sin," in *2015 IEEE 42nd Photovoltaic Specialist Conference (PVSC)*. IEEE, 2015, pp. 1–3.

[47] T. de Vrijer and B. Bouazzata, "degradation of a-/nc-ge:h films," 2021, current research; not published yet.

[48] A. Smets, Koper, and Smith, "Solar to products," Research Proposal, Delft University of Technology and Leiden University.